Rethinking the role of transport and photochemistry in regional ozone pollution: Insights from ozone mass and concentration budgets

Kun Qu[1], Xuesong Wang[2], Xuhui Cai[3], Yu Yan[4], Xipeng Jin[3], Mihalis Vrekoussis[5], Jin Shen[6], Teng Xiao[3], Limin Zeng[7], and Yuanghang Zhang[8]

[1]Peking Univeristy; University of Bremen
[2]College of Environmental Sciences and Engineering
[3]Peking University
[4]Peking university
[5]Institute of Environmental Physics, University of Bremen
[6]Guangdong Environmental Monitoring Center
[7]College of Environmental Sciences and Engineering, Peking University
[8]State Key Lab

November 23, 2022

Abstract

Understanding the role of transport and photochemistry is essential to alleviate regional ozone pollution. However, budget studies often report conflicting conclusions. Using the modeling results of WRF-CMAQ, we calculated the contributions of both processes to the variation of total ozone mass and mean ozone concentration (noted as ozone mass and concentration budget, respectively) within the atmospheric boundary layer (ABL) of the Pearl River Delta, China. Transport, especially the exchange between ABL and free troposphere, controls the ozone mass budget, whereas local photochemistry drives the rapid increase of ozone concentration in the daytime. Though transport has a limited effect on ozone concentration, its high contribution to the ozone mass budget determines that most ozone emanates from the outside regions. Consequently, the role of transport and photochemistry in ozone pollution may differ, depending on which of the two budgets is considered. Attention should be paid to budget type selections in future studies.

Rethinking the role of transport and photochemistry in regional ozone pollution: Insights from ozone mass and concentration budgets

K. Qu[1,2,3], X. Wang[1,2,*], X. Cai[1,2], Y. Yan[1,2], X. Jin[1,2], M. Vrekoussis[3,4,5], J. Shen[6], T. Xiao[1,2], L. Zeng[1,2] and Y. Zhang[1,2,7,8,*]

[1]State Key Joint Laboratory of Environmental Simulation and Pollution Control, College of Environmental Sciences and Engineering, Peking University, Beijing 100871, China.

[2]International Joint Laboratory for Regional Pollution Control, Ministry of Education, Beijing, 100816, China.

[3]Laboratory for Modeling and Observation of the Earth System (LAMOS), Institute of Environmental Physics (IUP), University of Bremen, Bremen, Germany.

[4]Center of Marine Environmental Sciences (MARUM), University of Bremen, Germany.

[5]Climate and Atmosphere Research Center (CARE-C), The Cyprus Institute, Cyprus.

[6]State Key Laboratory of Regional Air Quality Monitoring, Guangdong Key Laboratory of Secondary Air Pollution Research, Guangdong Environmental Monitoring Center, Guangzhou 510308, China.

[7]Beijing Innovation Center for Engineering Science and Advanced Technology, Peking University, Beijing 100871, China.

[8]CAS Center for Excellence in Regional Atmospheric Environment, Chinese Academy of Sciences, Xiamen 361021, China.

Corresponding author: X. Wang (xswang@pku.edu.cn) and Y. Zhang (yhzhang@pku.edu.cn)

Key Points:

- Regional ozone mass and concentration budgets were calculated based on WRF-CMAQ modeling results in the Pearl River Delta.
- Ozone mass budget is mainly controlled by transport, while ozone concentration budget is driven by photochemistry in the daytime.
- The difference between two budgets leads to conflicting conclusions about the role of transport and photochemistry in ozone pollution.

Abstract

Understanding the role of transport and photochemistry is essential to alleviate regional ozone pollution. However, budget studies often report conflicting conclusions. Using the modeling results of WRF-CMAQ, we calculated the contributions of both processes to the variation of total ozone mass and mean ozone concentration (noted as ozone mass and concentration budget, respectively) within the atmospheric boundary layer (ABL) of the Pearl River Delta, China. Transport, especially the exchange between ABL and free troposphere, controls the ozone mass budget, whereas local photochemistry drives the rapid increase of ozone concentration in the daytime. Though transport has a limited effect on ozone concentration, its high contribution to the ozone mass budget determines that most ozone emanates from the outside regions. Consequently, the role of transport and photochemistry in ozone pollution may differ, depending on which of the two budgets is considered. Attention should be paid to budget type selections in future studies.

Plain Language Summary

Ozone pollution occurs in many regions around the world. To tackle ozone pollution, it is needed to better understand and characterize processes that influence the variations of ozone, especially transport and daytime chemistry. However, reported studies often have different views on the relative importance of these two processes, which may limit their help for policy-makers to control ozone pollution effectively. We aim to answer why these studies report — at first glance — contradicting results. The WRF-CMAQ modeling results were used to calculate the influences of both processes on the changes of ozone mass and concentration in a typical city cluster. We found that transport controls the changes of ozone mass, but chemical processes contribute to the rapid increase of ozone concentration in the daytime. Although transport does not lead to big changes in ozone concentration, its high contribution to ozone mass increase explains why most ozone comes from the outside regions. The different influences of transport and daytime chemical processes on the changes of ozone mass and concentration seems to explain the contradicting views mentioned before. Future studies should be careful with that.

1 Introduction

Nowadays, many urban regions around the globe still experience tropospheric ozone (O_3) pollution (Schultz et al., 2017), which threatens human health, crop yields and ecosystem (Mills et al., 2013; Ainsworth, 2017; Zhang et al., 2019). High O_3 concentrations within a region are generally attributed to daytime photochemical production from O_3 precursors, i.e. NO_x (NO + NO_2) and volatile organic compounds (VOCs). However, since O_3 has a moderately long atmospheric lifetime (~ 22 d; Stevenson et al., 2006), transport, including horizontal transport (advection) and vertical exchange between atmospheric boundary layer (ABL) and free troposphere (FT) (entrainment and detrainment), may also contribute to high O_3 levels. To alleviate O_3 pollution effectively, it is required to understand the role of both processes during O_3-polluted periods.

Budget analysis provides valuable information to indicate the causes of regional O_3 pollution. O_3 budgets have been massively reported based on various observational and modeling methods, but they may come up with completely different conclusions. O_3 budgets based on in-situ (Su et al., 2018; Tan et al., 2018; Tan et al., 2019; Yu et al., 2020), aircraft measurements (Lenschow et al., 1981; Trousdell et al., 2016; Trousdell et al., 2019) and Process Analysis or alike modules in chemical transport models (CTMs) (Hou et al., 2014; Li et al., 2021; Yan et al., 2021) often suggest that O_3 production through local photochemistry drives the noon-time increase of O_3 concentration, whereas transport reduces O_3 over the same period. It does not mean that transport plays a less important role in O_3 pollution at every hour of the day; during several hours after sunrise, transport, especially ABL-FT exchange, may contribute to the rapid increase of O_3 levels (Kaser et al., 2017). However, in some studies (Memmesheimer et al., 1997; Lehning et al., 1998; Myriokefalitakis et al., 2016), O_3 transport fluxes are comparable to the contributions of photochemistry to O_3, suggesting that the influence of transport on O_3 pollution cannot be simply ignored. O_3 source apportionment using CTMs provides the contributions of emissions from different regions to O_3, thus it also serves as a tool for budget analysis. O_3 source apportionment results often showed that most O_3 emanates from non-local sources (Guo et al., 2018; Pay et al., 2019; Liu et al., 2020), emphasizing the dominant role of transport in O_3 pollution. Even for the same region and during the same season, conflicting O_3 budget results may be found, making policy-makers confused whether it is more effective to reduce emissions locally or on a larger

scale. Therefore, we must re-think the role of both transport and photochemistry in O_3 budget and explore why this discrepancy occurs.

In this study, we quantified the contributions of various processes (including transport and photochemistry) in regional O_3 budgets using the results from the Weather Research and Forecasting (WRF) and Community Multiscale Air Quality (CMAQ) models. The Pearl River Delta (PRD) region, a city cluster located on the southeast coast of China and exposed to severe O_3 pollution in summer and autumn (Gao et al., 2018), was selected as the targeted region in analysis. Since O_3 is well-mixed within the convective ABL during pollution (Tang et al., 2021), O_3 budgets within the ABL of the PRD are the focus of this study. Unlike using fixed values as in previous budget studies, here, the ABL heights were provided by the WRF modeling results. Thus, the volume defined by the grids below the ABL changes throughout the day. Two types of budgets were defined here, namely, O_3 mass and concentration budgets. They describe the contributions of processes to the variation of total O_3 mass and mean O_3 concentration, respectively, in the ABL of the PRD. The discrepancy between the aforementioned budget studies is hidden behind the difference between these two O_3 budgets.

2 Methodology: O_3 budget calculations

Figure 1 displays all processes considered in the O_3 budget calculations and the distributions of the PRD grids (lower-left panel), including the border grids (defined as the PRD grids adjacent to the outside regions). The contributions of horizontal transport through the borders of the PRD in four directions, ABL-FT exchange due to the changes of ABL height (marked as ABL-FT-H) and large-scale air motion (advection through the ABL top; marked as ABL-FT-M) were calculated using meteorological parameters and O_3 concentrations modeled by WRF-CMAQ. The contributions of gas-phase chemistry (including daytime photochemical O_3 production and O_3 titration by NO), cloud process (including below and in-cloud mixing, aqueous-phase chemistry, wet deposition; Liu et al., 2011) and dry deposition were provided by the Process Analysis results of CMAQ. Because diffusion near the boundaries and top of the region is expected to have a minor influence on the variation of O_3 mass and concentration, we did not involve it in O_3 budgets. The calculations of transport contributions in O_3 budgets are described in the following sections. More details about the calculation process are given in Text S1. (Note that the contributions to the O_3 mass variation per time are defined as O_3 fluxes.)

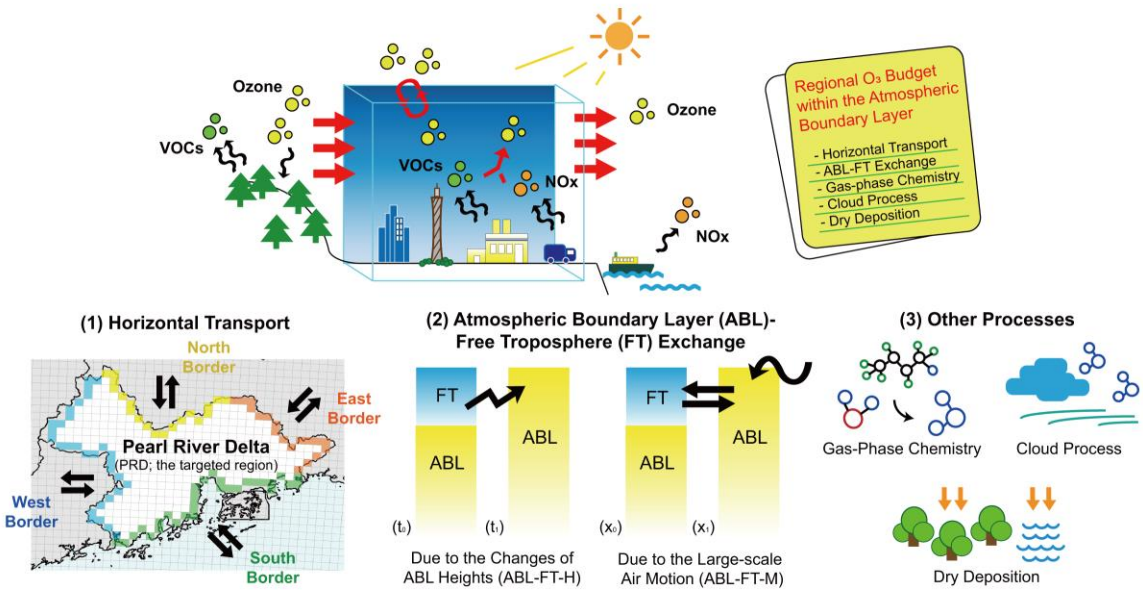

Figure 1. Schematic illustration of regional O_3 budgets (upper panel) and processes considered (lower panel): (1) Horizontal transport through the borders of the Pearl River Delta (PRD) in four directions (the distributions of the PRD grids are also shown (white for the non-border PRD grids; yellow, green, blue, orange for the north, south, west and east border grids, respectively)); (2) Exchange between atmospheric boundary layer (ABL) and free troposphere (FT), including the process due to the changes of ABL heights (ABL-FT-H) and large-scale air motion (ABL-FT-M); (3) Other processes, including gas-phase chemistry, cloud process and dry deposition.

2.1 Transport contributions in the O_3 mass budget

Using the method in Yang et al. (2012) and Chang et al. (2018), we calculated the horizontal transport fluxes of O_3. For instance, the O_3 flux attributed to the advection through the west interface of grid cells within the ABL (F_{htrans}) in the time interval dt is calculated as:

$$F_{htrans} = \int_0^H cuL\, dz\, dt \tag{1}$$

where c indicates O_3 concentration in the adjacent grid; u is the mean speed of the horizontal wind passing through the interface; L is the width of the grid cell (equal to the horizontal resolution of the model); dz is the height of vertical layers; H is the ABL height. The horizontal

transport fluxes of O_3 through every interface between one type of border and the outside regions were summed up as the net contribution of horizontal transport through that border in the O_3 mass budget.

ABL-FT exchange occurs through turbulence; thus, the quantification of its flux differs from that of horizontal transport flux (Zhang et al., 2018). The ABL-FT exchange flux of O_3 (F_{ABL-FT}) in the time interval dt is calculated as in Sinclair et al. (2010) and Jin et al. (2021):

$$\begin{aligned} F_{ABL-FT} &= F_{ABL-FT-H} + F_{ABL-FT-M} \\ &= c_h \frac{\partial H}{\partial t} L^2 dt + c_h \left(u_h \frac{\partial H}{\partial x} + v_h \frac{\partial H}{\partial y} - w_h \right) L^2 dt \end{aligned} \tag{2}$$

where c_h is the O_3 concentration in the ABL top; u_h, v_h and w_h are the ABL-top wind speeds in the x, y and z-direction, respectively. Two terms on the right-hand side of Eq. (2) separately describe the contributions of ABL-FT-H and ABL-FT-M (denoted separately as $F_{ABL-FT-H}$ and $F_{ABL-FT-M}$). The ABL-FT exchange fluxes of O_3 within all PRD grids were summed up as the net contributions of ABL-FT exchange in the O_3 mass budget.

2.2 Transport contributions in the O_3 concentration budget

The effects of transport on the variations of O_3 mass and concentration are different. According to the calculations in the last section, O_3 being transported into (out of) the region results in O_3 mass increase (decrease), which corresponds to a positive (negative) O_3 transport flux. However, whether O_3 concentration in the region increases or decreases also depends on the O_3 concentration in the transported air parcels. For instance, clean air parcels transported into the region dilute O_3 pollution and reduce O_3 concentration. Therefore, we applied different methods to quantify transport contributions in the O_3 concentration budget.

Suppose that an air parcel with a volume of dV is transported into the ABL of the PRD (its original volume is V) within a short time. For horizontal transport:

$$\left[\frac{\partial \langle c \rangle}{\partial t}\right]_{htrans} = \frac{F_{htrans} + \langle c \rangle (V - dV)}{V} - \langle c \rangle = \frac{F_{htrans} - \langle c \rangle dV}{V} \tag{3}$$

where $\langle c \rangle$ denotes mean O_3 concentration in the ABL of the PRD. The contributions of ABL-FT-M are quantified using a similar formula.

Through ABL-FT-H, air parcels in the FT are merged into (or segmented out of) the ABL, thus:

$$\left[\frac{\partial\langle c\rangle}{\partial t}\right]_{ABL-FT-H} = \frac{F_{ABL-FT-H} + \langle c\rangle V}{V + dV} - \langle c\rangle = \frac{F_{ABL-FT-H} - \langle c\rangle dV}{V + dV} \quad (4)$$

If the targeted region was small enough, Eqs. (3) and (4) would have the same forms as those used in 1-D models (Janssen and Pozzer, 2015; Vilà-Guerau de Arellano et al., 2015), which confirms the applicability of the above calculations (for details, see Text S2). For the hourly contributions of each process to O_3 concentration variations, their calculations are not trivial because V in Eqs. (3) and (4) may change notably within an hour. Therefore, we designed two calculation paths (Fig. S1):

a. O_3 mass change → ABL volume change;

b. ABL volume change → O_3 mass change.

where only O_3 mass or ABL volume changes in one calculation step. The contributions of ABL-FT-H are decomposed into two parts: ABL volume change during the ABL development (collapse) leads to lower (higher) O_3 concentration, and O_3 transported into the ABL (FT) leads to O_3 increase (decrease). These contributions are quantified separately in the ABL volume and O_3 mass change step. The contributions of other processes are quantified only in the O_3 mass change step. For one process, its contributions to O_3 concentration variations are calculated through both paths, and their mean value serves as an estimation close to its real contribution in the O_3 concentration budget.

2.3 Model setup and validation

The O_3 mass and concentration budgets within the ABL of the PRD were calculated based on the WRF-CMAQ modeling results by Qu et al. (2021). Two nested domains with the resolution of 36 and 12 km were set (denoted as d01 and d02 hereafter). The finer d02 modeling results were used in the O_3 budget calculations. October 2015 (October 11–November 10, 2015) and July 2016 (July 1–31, 2016) were selected as the representative months in autumn and summer, respectively, for the PRD. Here, O_3 polluted days are defined when the maximum 1-hr O_3 concentrations exceed 200 μg/m^3, or the maximum 8-hr average O_3 concentrations exceed 160 μg/m^3 (both are the Grade-II O_3 thresholds in the Chinese National Ambient Air Quality Standard) in any municipality of the PRD. According to this definition, there were 16 and 12 O_3 polluted days in two months, respectively (more information is given in Table S1). Further

discussions focus on the mean O_3 budgets of these days. The detailed setup of WRF-CMAQ, the valiadation of modeled meteorological parameters, O_3, NO_2 concentrations and hydrocarbons mixing ratios were introduced by Qu et al. (2021). Here, we also compared modeled ABL height, the vertical profiles of wind speed, direction and O_3 mixing ratio in Hong Kong (located in the south PRD) with corresponding observations from the IAGOS (In-service Aircraft for a Global Observing System; Petzold et al., 2015) dataset. As presented in Text S3, the acceptable modeling performance of these parameters indicates that the model provide reasonable initial data for the O_3 budget calculations.

If the calculation methods and assumptions were reasonable, the budget closure, or

$$\frac{\partial m(or\ \langle c \rangle)}{\partial t} - \left(S_{htrans} + S_{ABL-FT} + S_{chem} + S_{cloud} + S_{ddep}\right) = 0 \qquad (5)$$

would be achieved (S_{htrans}, S_{ABL-FT}, S_{chem}, S_{cloud} and S_{ddep} indicate the contributions of horizontal transport, ABL-FT exchange, gas-phase chemistry, cloud process and dry deposition, respectively, in O_3 budgets). Therefore, we used Eq. (5) to examine the validity of our calculations. The total O_3 mass at the start and end of each hour was directly used to calculate the hourly variations of O_3 mass. Besides these, volumes at these two moments (calculated using ABL heights in all PRD grids) were also used to calculate the hourly variations of O_3 concentration. As displayed in Fig. S2, the closure is met for O_3 mass and concentration budgets in both months, allowing for further analysis based on the quantified budgets.

2.4 Identifying source contributions in O_3 fluxes

It is generally believed that transport (gas-phase chemistry) is closely linked to the contributions of non-local (local) emissions for O_3, but quantitative evaluation of the connections between O_3 processes and sources is still lacking. By combining the O_3 budget calculation with the source apportionment method, the Brute Force Method (BFM; Clappier et al., 2017), we identified the regional contributions of O_3 fluxes attributed to transport and gas-phase chemistry. Of interest were the contributions of emissions in the PRD, other regions within d02 (mainly East and Central China, short for EC-China), and regions outside d02 (the boundary conditions (BCON) of d02 modeling). The distributions of these regions are shown in Fig. S3. Besides the base scenario, three sensitivity scenarios were simulated:

- The *PRD_zero* scenario: Emissions in the PRD were zeroed out;

- The *EC-China_zero* scenario: Emissions in the EC-China were zeroed out;
- The *All_zero* scenario: All emissions within d02 were shut down.

For the process i, its O_3 fluxes in the base scenario and three sensitivity scenarios were quantified using the same method introduced in Sect. 2.1, denoted as $f_{i,base}$, f_{i,PRD_zero}, $f_{i,EC-China\_zero}$, and f_{i,all_zero}, respectively. Then, the contributions of PRD, EC-China and BCON in O_3 fluxes attributed to the process i (separately denoted as $F_{i,PRD}$, $F_{i,EC-China}$, and $F_{i,BCON}$) were calculated as follows:

$$F_{i,PRD} = \frac{1}{2}[(f_{i,base} - f_{i,PRD\_zero}) + (f_{i,EC-China\_zero} - f_{i,all\_zero})] \quad (6)$$

$$F_{i,EC-China} = \frac{1}{2}[(f_{i,base} - f_{i,EC-China\_zero}) + (f_{i,PRD\_zero} - f_{i,all\_zero})] \quad (7)$$

$$F_{i,BCON} = f_{i,all\_zero} \quad (8)$$

In Eq. (6-7), the contributions of emissions are calculated as the average results of these using top-down BFM ($(f_{i,base} - f_{i,PRD\_zero})$, $(f_{i,base} - f_{i,EC-China\_zero})$ for the PRD and EC-China emissions, respectively) and bottom-up BFM ($(f_{i,EC-China\_zero} - f_{i,all\_zero})$, $(f_{i,PRD\_zero} - f_{i,all\_zero})$ for the PRD and EC-China emissions, respectively). By doing so, the non-additivity (the sum of contributions is not equal to the concerned metric) caused by the non-linearity between O_3 and precursors can be avoided (Qu et al., 2021).

3 Results

3.1 O_3 mass budget

The diurnal changes of the O_3 mass budget within the ABL of the PRD are shown in the upper panels of Fig. 2. In both autumn and summer, total O_3 mass increased after sunrise (~6:00 local time (LT) in autumn, ~5:00 LT in summer) until noon (~14:00 LT), then decreased rapidly in the afternoon and remained stable at night. The change of total O_3 mass agrees well with the diurnal cycle of ABL (Lee, 2015) — daytime ABL development (collapse) and notable O_3 mass increase (decrease) nearly occur simultaneously, and the negligible changes of O_3 mass at night may be related to the small variations of stable ABL.

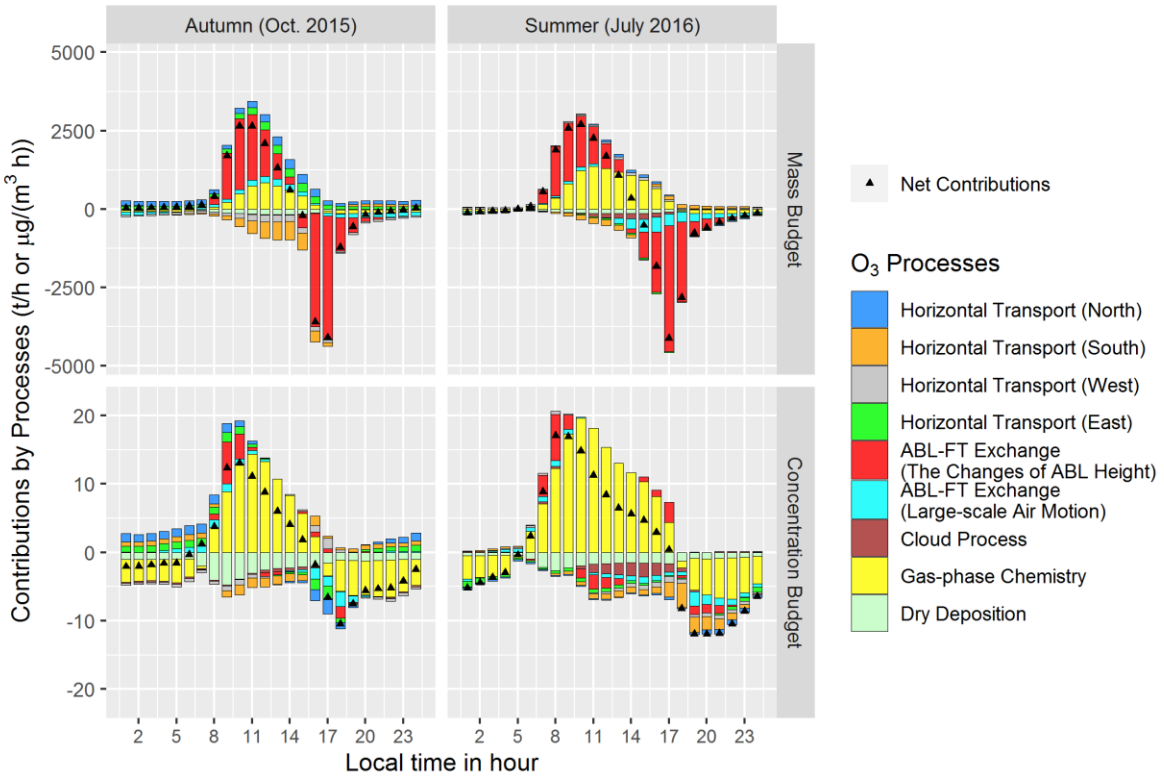

Figure 2. Mean diurnal changes of O_3 mass budget (upper panels) and concentration budget (lower panels) on the polluted days of representative months in autumn (Oct. 2015; left panels) and summer (July 2016; right panels) within the atmospheric boundary layer (ABL) of the Pearl River Delta. FT, free troposphere. The units for the O_3 mass and concentration budgets are t/h and μg/(m^3 h), respectively.

The contribution of processes to the variation of O_3 mass highlights the prominent role of transport. On average, it contributed to 78% and 53% of the O_3 mass increase during the O_3-increasing hours in autumn (6:00-14:00 LT) and summer (5:00-14:00 LT), respectively, and over 90% of the O_3 mass decrease during the O_3-reducing hours in both seasons (14:00-19:00 LT in autumn, 14:00-20:00 LT in summer). Most O_3 was transported into or out of the PRD through ABL-FT-H, which explains the consistency between the changes of O_3 mass and ABL. The influences of ABL-FT-M and horizontal transport on O_3 mass were relatively limited (more analyses are given in Text S4). Gas-phase chemistry (photochemistry) also contributed to the increasing O_3 mass during the daytime, especially in summer. However, its mean contribution

during the O_3-increasing hours (22% in autumn, 47% in summer) was lower than transport. Cloud process and dry deposition acted as O_3 sinks with negligible contributions in the O_3 mass budget. In summary, for the O_3 mass budget, transport tends to be more important than photochemistry.

The O_3 mass budget in this study agrees well with our common understanding of O_3 processes. The main role of transport (ABL-FT exchange) in the O_3 mass budget reflects the influence of the ABL diurnal cycle on regional O_3 pollution. In particular, massive O_3 being transported into the ABL during the O_3-increasing hours is critical for the characteristics of O_3 pollution, including O_3 sources, which is further discussed in Sect. 3.3.

3.2 O_3 concentration budget

The diurnal changes of mean O_3 concentration within the ABL of the PRD (Fig. 2, lower panels) differ from these of O_3 mass — O_3 concentration increased during most daytime hours, and its reduction at night was also considerable. We compared the ABL-mean O_3 concentration with observed and modeled mean near-ground O_3 concentrations in 18 sites of the Guangdong-Hong Kong-Macao PRD Regional Air Quality Monitoring Network (their distributions are shown in Fig. S4). As presented in Fig S5, three types of O_3 concentration feature with similar diurnal changes. Thus, the budget of ABL-mean O_3 concentration can illustrate more general causes of near-ground O_3 pollution in the PRD.

Unlike the main role of transport for the O_3 mass budget, gas-phase chemistry controlled almost exclusively the O_3 concentration budget. During the O_3-increasing hours defined in the last section, gas-phase chemistry (photochemistry) contributed to 74% and 95% of the O_3 concentration increase in autumn and summer, respectively, which are notably higher than the contributions of transport (25% in autumn, 5% in summer). It also led to the O_3 concentration decrease at night, suggesting that O_3 were titrated by NO. A considerable contribution of transport (mainly ABL-FT-H) to the O_3 increase is found mainly during 2-3 hours after sunrise (highest hourly contributions are ~40%, ~25% in autumn and summer, respectively), indicating that air masses containing high-level O_3 were entrained from residual layers. ABL-FT-M and horizontal transport may increase or decrease ABL-mean O_3 concentration, depending on the O_3 levels in air parcels transported into and out of the region (more analyses are given in Text S4). But during most hours in the daytime, these two transport processes had only a limited influence

on O_3 concentration variations. What is also different for the O_3 concentration budget compared to its mass budget is that dry deposition served as the major sink process for O_3 in the daytime, contributing to non-negligible O_3 concentration decreases. These results indicate that gas-phase chemistry played a major role in the variations of O_3 concentrations. In particular, photochemistry led to the rapid formation of O_3 pollution in the daytime. Our conclusions agree well with those in previous O_3 concentration budgets publications (Lenschow et al., 1981; Hou et al., 2014; Trousdell et al., 2016; Su et al., 2018; Tan et al., 2018; Tan et al., 2019; Trousdell et al., 2019; Yu et al., 2020; Li et al., 2021; Yan et al., 2021).

3.3 The sources of O_3 fluxes

Typically, non-local sources contributed to most O_3 in the PRD (Li et al., 2012; Li et al., 2013; Yang et al., 2019; Gao et al., 2020). This is also the case for the O_3 polluted days in the representative months of autumn and summer, when non-local sources contributed on average to 89% and 65% of the O_3 in the PRD, respectively, during 9:00-17:00 LT (55% and 32% contributed by BCON, 34% and 33% contributed by EC-China in two months; Qu et al., 2021). To explain why non-local O_3 sources are dominant for the PRD, we identified the regional sources of O_3 fluxes attributed to ABL-FT exchange, horizontal transport and gas-phase chemistry (Fig. 3; the results within 5:00-20:00 LT are shown). Since apparently, O_3 transported out of the PRD does not influence O_3 sources within the region, we mainly focus on the source of O_3 transported into the PRD (or O_3 influxes) in the discussions.

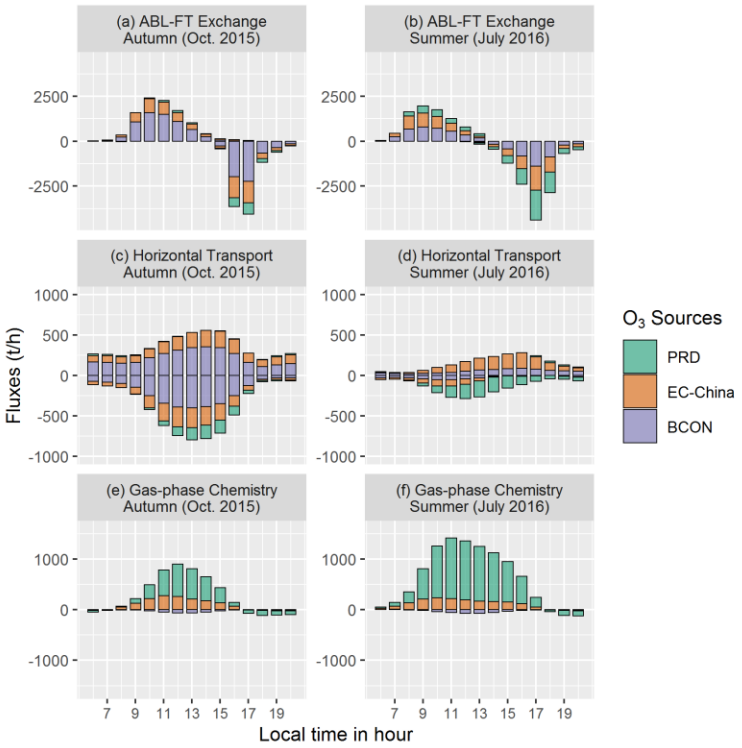

Figure 3. Mean diurnal changes of the sources of O_3 fluxes attributed to (a-b) ABL-FT exchange, (c-d) horizontal transport, and (e-f) gas-phase chemistry on the polluted days of representative months in autumn (Oct. 2015; a,c,e) and summer (July 2016; b,d,f). The results within 5:00-20:00 LT are shown here. ABL, atmospheric boundary layer; FT, free troposphere; PRD, Pearl River Delta; EC-China, East and Central China; BCON, the boundary conditions of d02 modeling, or the contribution of sources outside d02.

ABL-FT exchange, the process with the highest O_3 fluxes, was mainly related to the contributions from non-local emissions. In autumn, the contributions of BCON and EC-China accounted for 65% and 31%, respectively, in O_3 influxes during the O_3-increasing hours. By contrast, local emissions contributed to only 4% of the O_3 influxes during the same period. Thus, local O_3 recirculation had a limited influence on O_3 pollution. The results in summer were similar to those in autumn, except that the contributions of PRD and EC-China emissions were higher in O_3 influxes. Especially, local contributions accounted for 20% of the O_3 influxes during the O_3-increasing hours, but still lower than non-local contributions (38%, 42% for EC-China and BCON, respectively).

O_3 fluxes attributed to horizontal transport were connected to the contribution of non-local sources as well. In both seasons, O_3 transported into the PRD originated nearly all from non-local sources.

It is not surprising that most O_3 produced through gas-phase chemistry (photochemistry) was related to local contributions (accounting for 66% and 82% during the daytime of autumn (6:00-19:00 LT) and summer (5:00-20:00 LT), respectively). However, the contributions of EC-China reached 34% and 18% in two seasons, respectively, indicating the considerable influence of precursor transport.

O_3 source has close connections with the O_3 mass budget. Accumulated net O_3 flux during the O_3-increasing hours exceeded 10000 t in the PRD, which is 6-9 times of the original O_3 mass before sunrise (< 1500 t). Thus, daytime O_3 sources within the region were nearly determined by the sources of these newly transported or produced O_3. High O_3 fluxes attributed to transport (ABL-FT exchange) and the dominance of non-local sources in these fluxes ensured that most O_3 in the PRD was contributed by non-local sources. The reduced non-local contributions to O_3 in summer than autumn can be explained as the combined effects of higher O_3 photochemical fluxes, lower non-local contributions in O_3 photochemical fluxes and higher local contributions in O_3 transport fluxes. In the O_3 concentration budget, transport had relatively limited effects on O_3 concentration increase compared to photochemistry, making it less important for O_3. Therefore, the difference between O_3 mass and concentration budgets potentially results in diverse understandings about the role of transport and photochemistry in regional O_3 pollution.

4 Discussion and conclusion

Reported O_3 budget studies often concluded with a conflicting role of transport and photochemistry in O_3 pollution. To explore its causes, we used the modeling results of WRF-CMAQ to quantify their contributions in the O_3 mass and concentration budgets. Results in the PRD revealed that transport, especially ABL-FT exchange, is the main process contributing to O_3 mass increase in the morning (78%, 53% in autumn and summer, respectively) and its decrease in the afternoon (> 90%). Gas-phase chemistry, including daytime photochemistry and nighttime O_3 titration, drives the variations of O_3 concentration. Although massive O_3 transported into the ABL in the morning has a limited influence on O_3 concentration increase (25%, 5% in autumn and summer, respectively), it determines the dominance of non-local

sources for O_3 in the PRD. The difference between two O_3 budgets could lead to different understandings about the role of transport and photochemistry in regional O_3 pollution.

Different results from two O_3 budgets are attributed to two reasons. Firstly, transport has distinct effects on the variation of O_3 mass and concentration — O_3 transported into (out of) the studied region has a positive (negative) contribution to O_3 mass, but its contribution to the variation of O_3 concentration also depends on the O_3 levels in the transported air parcels. This has been considered in the budget calculations introduced in Sect. 2. The second reason is that ABL undergoes rapid diurnal changes, especially in the daytime. In different hours, similar contributions to O_3 mass within different ABL volumes can easily correspond to distinct contributions to O_3 concentration. The conclusions of this study are also applicable to other pollutants with moderately long atmospheric lifetimes, such as $PM_{2.5}$. Transport and chemical processes are both important for these pollutants but with different influences on their mass and concentration, which should be considered in the analyses.

Uncertainty remains in the calculated O_3 budgets, which is likely related to the biases in the modeling results. Therefore, supporting observations are essential for future research. Recent progress in observational techniques (Zhao et al., 2021; Zhou et al., 2021) has enabled three-dimensional measurements of meteorological parameters and O_3 concentrations with high spatiotemporal resolution and coverage. These data can be used not only in the model validation of key parameters in budget calculations, but also in the comparisons between observation- and modeling-based contributions by various processes in O_3 budgets. By doing so, more accurate O_3 budgets will be obtained.

This study concluded that transport and gas-phase chemistry separately play the main role in O_3 mass and concentration budgets. Therefore, attention should be paid to selecting a proper budget type and using correct calculation methods in related research. Based on two O_3 budgets, we suggest that emission reduction in the upwind regions can effectively lower daily-mean O_3 levels due to its high contributions to regional O_3, but a longer time is needed due to the slow response of O_3 concentration to transport. By contrast, reducing local emissions hinders rapid daytime O_3 concentration increase and lowers O_3 peak levels efficiently in the short term. The choice of which strategy to apply depends on the specific goals of O_3 control (mean levels vs. peak levels;

long-term vs. short-term), which are set based on more in-depth understanding of the O_3 effect on human health, crop yields and ecosystem.

Acknowledgments

This study was supported by the National Key Research and Development Program of China (grant No. 2018YFC0213204), the National Science and Technology Pillar Program of China (grant No. 2014BAC21B01) and the co-funded DFG-NSFC Sino-German AirChanges project (grant No. 448720203).

Open Research

The source codes of WRF and CMAQ are availiable at the site https://www2.mmm.ucar.edu/wrf/users/download/get_sources.html and https://www.cmascenter.org/cmaq/, respectively. FNL meteorological input files were downloaded from the site https://rda.ucar.edu/datasets/ds083.2/. MEIC v1.3 anthropogenic emission inventory is available at http://meicmodel.org/. The source codes of MEGAN can be found at https://bai.ess.uci.edu/megan/data-and-code. IAGOS dataset used in model validation was downloaded from http://iagos-data.fr/. We also provided the initial Fortran code used in ozone budget calculations and hourly O_3 mass and concentration budget results in two representative months (the initial data of Fig. 2) at https://doi.org/10.5281/zenodo.6259253.

References

Ainsworth, E. A. (2017). Understanding and improving global crop response to ozone pollution. *The Plant Journal*, 90(5), 886-897. doi: https://doi.org/10.1111/tpj.13298

Chang, X., Wang, S., Zhao, B., Cai, S., & Hao, J. (2018). Assessment of inter-city transport of particulate matter in the Beijing–Tianjin–Hebei region. *Atmospheric Chemistry and Physics*, 18(7), 4843-4858. doi: https://doi.org/10.5194/acp-18-4843-2018

Clappier, A., Belis, C. A., Pernigotti, D., & Thunis, P. (2017). Source apportionment and sensitivity analysis: two methodologies with two different purposes. Geoscientific Model Development, 10(11), 4245-4256. doi: https://doi.org/10.5194/gmd-10-4245-2017

Gao, M., Gao, J., Zhu, B., Kumar, R., Lu, X., Song, S., Zhang, Y., Jia, B., Wang, P., Beig, G., Hu, J., Ying, Q., Zhang, H., Sherman, P., & McElroy, M. B. (2020). Ozone pollution over China and India: seasonality and sources. *Atmospheric Chemistry and Physics*, 20(7), 4399-4414. doi: https://doi.org/10.5194/acp-20-4399-2020

Gao, X., Deng, X., Tan, H., Wang, C., Wang, N., & Yue, D. (2018). Characteristics and analysis on regional pollution process and circulation weather types over Guangdong Province (in Chinese). *Acta Scientiae Circumstantiae*, 38, 1708–1716. doi: https://doi.org/10.13671/j.hjkxxb.2017.0473

Guo, J. J., Fiore, A. M., Murray, L. T., Jaffe, D. A., Schnell, J. L., Moore, C. T., & Milly, G. P. (2018). Average versus high surface ozone levels over the continental USA: model bias, background influences, and interannual variability. *Atmospheric Chemistry and Physics*, 18(16), 12123-12140. doi: https://doi.org/10.5194/acp-18-12123-2018

Hou, X., Zhu, B., Kang, H., & Gao, J. (2014). Analysis of seasonal ozone budget and spring ozone latitudinal gradient variation in the boundary layer of the Asia-Pacific region. *Atmospheric Environment*, 94, 734-741. doi: https://doi.org/10.1016/j.atmosenv.2014.06.006

Janssen, R. H. H., & Pozzer, A. (2015). Description and implementation of a MiXed Layer model (MXL, v1.0) for the dynamics of the atmospheric boundary layer in the Modular Earth Submodel System (MESSy). *Geoscientific Model Development*, 8(3), 453-471. doi: https://doi.org/10.5194/gmd-8-453-2015

Jin, X., Cai, X., Huang, Q., Wang, X., Song, Y., & Zhu, T. (2021). Atmospheric Boundary Layer-Free Troposphere Air Exchange in the North China Plain and its Impact on $PM_{2.5}$ Pollution. *Journal of Geophysical Research: Atmospheres*, 126(9), e2021JD034641. doi: https://doi.org/10.1029/2021JD034641

Kaser, L., Patton, E. G., Pfister, G. G., Weinheimer, A. J., Montzka, D. D., Flocke, F., Thompson, A. M., Stauffer, H. S., & Halliday, H. S. (2017). The effect of entrainment through atmospheric boundary layer growth on observed and modeled surface ozone in the Colorado Front Range. *Journal of Geophysical Research: Atmospheres*, 122(11), 6075-6093. doi: https://doi.org/10.1002/2016JD026245

Lee, X. (2018). Fundamentals of Boundary-Layer Meteorology. (Vol. 256). Springer International Publishing.

Lehning, M., Richner, H., Kok, G. L., & Neininger, B. (1998). Vertical exchange and regional budgets of air pollutants over densely populated areas. *Atmospheric Environment*, 32(8), 1353-1363. doi: https://doi.org/10.1016/S1352-2310(97)00249-5

Lenschow, D. H., Pearson Jr, R., & Stankov, B. B. (1981). Estimating the ozone budget in the boundary layer by use of aircraft measurements of ozone eddy flux and mean concentration. *Journal of Geophysical Research: Oceans*, 86(C8), 7291-7297. doi: https://doi.org/10.1029/JC086iC08p07291

Li, L., Xie, F., Li, J., Gong, K., Xie, X., Qin, Y., Qin, M., & Hu, J. (2021). Diagnostic analysis of regional ozone pollution in Yangtze River Delta, China: A case study in summer 2020. *Science of The Total Environment*, 151511. doi: https://doi.org/10.1016/j.scitotenv.2021.151511

Li, Y., Lau, A. K., Fung, J. C., Ma, H., & Tse, Y. (2013). Systematic evaluation of ozone control policies using an Ozone Source Apportionment method. *Atmospheric Environment*, 76, 136-146. doi: https://doi.org/10.1016/j.atmosenv.2013.02.033

Li, Y., Lau, A. H., Fung, J. H., Zheng, J. Y., Zhong, L. J., & Louie, P. K. K. (2012). Ozone source apportionment (OSAT) to differentiate local regional and super-regional source contributions in the Pearl River Delta region, China. *Journal of Geophysical Research: Atmospheres*, 117(D15). doi: https://doi.org/10.1029/2011JD017340

Liu, H., Zhang, M., & Han, X. (2020). A review of surface ozone source apportionment in China. *Atmospheric and Oceanic Science Letters*, 13(5), 470-484. doi: https://doi.org/10.1080/16742834.2020.1768025

Liu, P., Zhang, Y., Yu, S., & Schere, K. L. (2011). Use of a process analysis tool for diagnostic study on fine particulate matter predictions in the US–Part II: Analyses and sensitivity simulations. *Atmospheric Pollution Research*, 2(1), 61-71. doi: https://doi.org/10.5094/APR.2011.008

Memmesheimer, M., Ebel, A., & Roemer, M. (1997). Budget calculations for ozone and its precursors: Seasonal and episodic features based on model simulations. *Journal of Atmospheric Chemistry*, 28(1), 283-317. doi: https://doi.org/10.1023/A:1005815212628

Mills, G., Wagg, S., & Harmens, H. (Eds.). (2013). Ozone Pollution: impacts on ecosystem services and biodiversity. Bangor, UK, NERC/Centre for Ecology & Hydrology, 104pp. (CEH Project no. C04062, C04325)

Myriokefalitakis, S., Daskalakis, N., Fanourgakis, G. S., Voulgarakis, A., Krol, M. C., de Brugh, J. A., & Kanakidou, M. (2016). Ozone and carbon monoxide budgets over the Eastern Mediterranean. *Science of the Total Environment*, 563, 40-52. doi: https://doi.org/10.1016/j.scitotenv.2016.04.061

Pay, M. T., Gangoiti, G., Guevara, M., Napelenok, S., Querol, X., Jorba, O., & Pérez García-Pando, C. (2019). Ozone source apportionment during peak summer events over southwestern Europe. *Atmospheric Chemistry and Physics*, 19(8), 5467-5494. doi: https://doi.org/10.5194/acp-19-5467-2019

Petzold, A., Thouret, V., Gerbig, C., Zahn, A., Brenninkmeijer, C. A., Gallagher, M., Hermann, M., Pontaud M., Ziereis, H., Boulanger, D., Marshall, J., Nédélec, P., Smit, H. G. J., Friess, U., Flaud, J.-M., Wahner, A., Cammas, J.-P., Volz-Thomas, A., & IAGOS TEAM. (2015). Global-scale atmosphere monitoring by in-service aircraft–current achievements and future prospects of the European Research Infrastructure IAGOS. *Tellus B: Chemical and Physical Meteorology*, 67(1), 28452. doi: https://doi.org/10.3402/tellusb.v67.28452

Qu, K., Wang, X., Yan, Y., Shen, J., Xiao, T., Dong, H., Zeng, L., & Zhang, Y. (2021). A comparative study to reveal the influence of typhoons on the transport, production and accumulation of O_3 in the Pearl River Delta, China. *Atmospheric Chemistry and Physics*, 21(15), 11593-11612. doi: https://doi.org/10.5194/acp-21-11593-2021

Schultz, M. G., Schröder, S., Lyapina, O., Cooper, O., Galbally, I., Petropavlovskikh, I., Von Schneidemesser, E., Tanimoto, H., Elshorbany, Y., Naja, M., Seguel, R., Dauert, U., Eckhardt, P., Feigenspahn, S., Fiebig, M., Hjellbrekke, A.-G., Hong, Y.-D., Kjeld, P. C., Koide, H., Lear, G., Tarasick, D., Ueno, M., Wallasch, M., Baumgardner, D., Chuang, M.-T., Gillett, R., Lee, M., Molloy, S., Moolla, R., Wang, T., Sharps, K., Adame, J. A., Ancellet, G., Apadula, F., Artaxo, P., Barlasina, M., Bogucka, M., Bonasoni, P., Chang, L., Colomb, A., Cuevas, E., Cupeiro, M., Degorska, A., Ding, A., Fröhlich, M., Frolova, M., Gadhavi, H., Gheusi, F., Gilge, S., Gonzalez, M. Y., Gros, V., Hamad, S. H., Helmig, D., Henriques, D., Hermansen, O., Holla, R., Huber, J., Im, U., Jaffe, D. A., Komala, N., Kubistin, D., Lam, K.-S., Laurila, T., Lee, H., Levy, I., Mazzoleni, C., Mazzoleni, L., McClure-Begley, A., Mohamad, M., Murovic, M., Navarro-Comas, M., Nicodim, F., Parrish, D., Read, K. A., Reid, N., Ries, L., Saxena, P., Schwab, J. J., Scorgie, Y., Senik, I., Simmonds, P., Sinha, V., Skorokhod, A., Spain, G., Spangl, W., Spoor, R., Springston, S. R., Steer, K., Steinbacher, M., Suharguniyawan, E., Torre, P., Trickl, T., Weili, L., Weller, R., Xu, X., Xue, L., & Zhiqiang, M. (2017). Tropospheric ozone assessment report: Database and metrics data of global surface ozone observations. *Elementa Science of the Anthropocene*, 5, 58. doi: https://doi.org/10.1525/elementa.244

Sinclair, V. A., Belcher, S. E., & Gray, S. L. (2010). Synoptic controls on boundary-layer characteristics. *Boundary-layer meteorology*, 134(3), 387-409. doi: https://doi.org/10.1007/s10546-009-9455-6

Stevenson, D. S., Dentener, F. J., Schultz, M. G., Ellingsen, K., van Noije, T. P. C., Wild, O., Zeng, G., Amann, M., therton, C. S., Bell, N., Bergmann, D. J., Bey, I., Butler, T., Cofala, J., Collins, W. J., Derwent, R. G., Doherty, R. M., Drevet, J., Eskes, H. J., Fiore,

A. M., Gauss, M., Hauglustaine, D. A., Horowitz, L. W., Isaksen, I. S. A., Krol, M. C., Lamarque, J.-F., Lawrence, M. G., Montanaro, V., Müller, J.-F., Pitari, G., Prather, M. J., Pyle, J. A., Rast, S., Rodriguez, J. M., Sanderson, M. G., Savage, N. H., Shindell, D. T., Strahan, S. E., Sudo, K., & Szopa, S. (2006). Multimodel ensemble simulations of present-day and near-future tropospheric ozone. *Journal of Geophysical Research*, 111, D08301. doi: https://doi.org/10.1029/2005JD006338

Su, R., Lu, K., Yu, J., Tan, Z., Jiang, M., Li, J., Xie, S., Wu, Y., Zeng, L., Zhai, C., & Zhang, Y. (2018). Exploration of the formation mechanism and source attribution of ambient ozone in Chongqing with an observation-based model. *Science China Earth Sciences*, 61(1), 23-32. doi: https://doi.org/10.1007/s11430-017-9104-9

Tan, Z., Lu, K., Jiang, M., Su, R., Dong, H., Zeng, L., Xie, S., Tan, Q., & Zhang, Y. (2018). Exploring ozone pollution in Chengdu, southwestern China: A case study from radical chemistry to O_3-VOC-NO_x sensitivity. *Science of the Total Environment*, 636, 775-786. doi: https://doi.org/10.1016/j.scitotenv.2018.04.286

Tan, Z., Lu, K., Jiang, M., Su, R., Wang, H., Lou, S., Fu, Q., Zhai, C., Tan, Q., Yue, D., Chen, D., Wang, Z., Xie, S., Zeng, L., & Zhang, Y. (2019). Daytime atmospheric oxidation capacity in four Chinese megacities during the photochemically polluted season: a case study based on box model simulation. *Atmospheric Chemistry and Physics*, 19(6), 3493-3513. doi: https://doi.org/10.5194/acp-19-3493-2019

Tang, G., Liu, Y., Huang, X., Wang, Y., Hu, B., Zhang, Y., Hu, B., Zhang, Y., Song, T., Li, X., Wu, S., Li, Q., Kang, Y., Zhu, Z., Wang, M., Wang, Y., Li, T., Li, X., & Wang, Y. (2021). Aggravated ozone pollution in the strong free convection boundary layer. *Science*

of The Total Environment, 788, 147740. doi: https://doi.org/10.1016/j.scitotenv.2021.147740

Trousdell, J. F., Caputi, D., Smoot, J., Conley, S. A., & Faloona, I. C. (2019). Photochemical production of ozone and emissions of NO_x and CH_4 in the San Joaquin Valley. *Atmospheric Chemistry and Physics*, 19(16), 10697-10716. doi: https://doi.org/10.5194/acp-19-10697-2019

Trousdell, J. F., Conley, S. A., Post, A., & Faloona, I. C. (2016). Observing entrainment mixing, photochemical ozone production, and regional methane emissions by aircraft using a simple mixed-layer framework. *Atmospheric Chemistry and Physics*, 16(24), 15433-15450. doi: https://doi.org/10.5194/acp-16-15433-2016

Vilà-Guerau de Arellano, J., Van Heerwaarden, C. C., Van Stratum, B. J., & Van den Dries, K. (2015). Atmospheric boundary layer: Integrating air chemistry and land interactions. Cambridge University Press.

Yan, F., Gao, Y., Ma, M., Liu, C., Ji, X., Zhao, F., Yao, X., & Gao, H. (2021). Revealing the modulation of boundary conditions and governing processes on ozone formation over northern China in June 2017. *Environmental Pollution*, 272, 115999. doi: https://doi.org/10.1016/j.envpol.2020.115999

Yang, L., Wang, X., & Chen, Q. (2012). New method for investigating regional interactions of air pollutants (in Chinese). *Acta Scientiae Circumstantiae*, 32(3), 528-536. doi: https://doi.org/10.13671/j.hjkxxb.2012.03.012

Yang, W., Chen, H., Wang, W., Wu, J., Li, J., Wang, Z., Zheng, J., & Chen, D. (2019). Modeling study of ozone source apportionment over the Pearl River Delta in 2015. *Environmental Pollution*, 253, 393-402. doi: https://doi.org/10.1016/j.envpol.2019.06.091

Yu, D., Tan, Z., Lu, K., Ma, X., Li, X., Chen, S., Zhu, B., Lin, L., Li, Y., Qiu, P., Yang, X., Liu, Y., Wang, H., He, L., Huang, X., & Zhang, Y. (2020). An explicit study of local ozone budget and NO_x-VOCs sensitivity in Shenzhen China. *Atmospheric Environment*, 224, 117304. doi: https://doi.org/10.1016/j.atmosenv.2020.117304

Zhang, H., Zhou, X., Zou, J., Wang, W., Xue, L., Ding, Q., Wang, X., Zhang, N., Ding, A., Sun, J., & Wang, W. (2018). A review on the methods for observing the substance and energy exchange between atmosphere boundary layer and free troposphere. *Atmosphere*, 9(12), 460. doi: https://doi.org/10.3390/atmos9120460

Zhang, J. J., Wei, Y., & Fang, Z. (2019). Ozone pollution: a major health hazard worldwide. *Frontiers in immunology*, 10, 2518. doi: https://doi.org/10.3389/fimmu.2019.02518

Zhao, R., Hu, Q., Sun, Z., Wu, Y., Xing, C., Liu, H., & Liu, C. (2021). Review of Space and Ground Integrated Remote Sensing for Air Pollutants (in Chinese). *Research of Environmental Sciences*, 34(1), 28-40. doi: https://doi.org/10.13198/j.issn.1001-6929.2020.11.25

Zhou, B., Zhang, S., Xue, R., Li, J., & Wang, S. (2021). A review of Space-Air-Ground integrated remote sensing techniques for atmospheric monitoring. *Journal of Environmental Sciences*. doi: https://doi.org/10.1016/j.jes.2021.12.008

References From the Supporting Infomation

Chan, R. L. M., Lee, O. S. M., & Cheng, A. Y. S. (2006). Diurnal variation of mixing height in Hong Kong. In Reviewed and revised papers presented at the 23rd International Laser Radar Conference (pp. 737-740).

Dai, C., Wang, Q., Kalogiros, J. A., Lenschow, D. H., Gao, Z., & Zhou, M. (2014). Determining boundary-layer height from aircraft measurements. *Boundary-layer meteorology*, 152(3), 277-302. doi: https://doi.org/10.1007/s10546-014-9929-z

Ding, A., Wang, T., Zhao, M., Wang, T., & Li, Z. (2004). Simulation of sea-land breezes and a discussion of their implications on the transport of air pollution during a multi-day ozone episode in the Pearl River Delta of China. *Atmospheric Environment*, 38(39), 6737-6750. doi: https://doi.org/10.1016/j.atmosenv.2004.09.017

Fan, S. J., Fan, Q., Yu, W., Luo, X. Y., Wang, B. M., Song, L. L., & Leong, K. L. (2011). Atmospheric boundary layer characteristics over the Pearl River Delta, China, during the summer of 2006: measurement and model results. *Atmospheric Chemistry and Physics*, 11(13), 6297-6310. doi: https://doi.org/10.5194/acp-11-6297-2011

He, G., Deng, T., Wu, D., Wu, C., Huang, X., Li, Z., Yin, C., Zou, Y., Song, L., Ouyang, S., Tao, L., & Zhang, X. (2021). Characteristics of boundary layer ozone and its effect on surface ozone concentration in Shenzhen, China: A case study. *Science of The Total Environment*, 148044. doi: https://doi.org/10.1016/j.scitotenv.2021.148044

Janssen, R. H. H., & Pozzer, A. (2015). Description and implementation of a MiXed Layer model (MXL, v1.0) for the dynamics of the atmospheric boundary layer in the Modular Earth Submodel System (MESSy). *Geoscientific Model Development*, 8(3), 453-471. doi: https://doi.org/10.5194/gmd-8-453-2015

Petzold, A., Thouret, V., Gerbig, C., Zahn, A., Brenninkmeijer, C. A., Gallagher, M., Hermann, M., Pontaud M., Ziereis, H., Boulanger, D., Marshall, J., Nédélec, P., Smit, H. G. J., Friess, U., Flaud, J.-M., Wahner, A., Cammas, J.-P., Volz-Thomas, A., & IAGOS TEAM. (2015). Global-scale atmosphere monitoring by in-service aircraft–current

achievements and future prospects of the European Research Infrastructure IAGOS. *Tellus B: Chemical and Physical Meteorology*, 67(1), 28452. doi: https://doi.org/10.3402/tellusb.v67.28452

Qu, K., Wang, X., Yan, Y., Shen, J., Xiao, T., Dong, H., Zeng, L., & Zhang, Y. (2021). A comparative study to reveal the influence of typhoons on the transport, production and accumulation of O_3 in the Pearl River Delta, China. *Atmospheric Chemistry and Physics*, 21(15), 11593-11612. doi: https://doi.org/10.5194/acp-21-11593-2021

Song, L., Deng, T., Li, Z. N., Wu, C., He, G. W., Li, F., Wu, M., & Wu, D. (2021). Retrieval of Boundary Layer Height and Its Influence on PM2.5 Concentration Based on Lidar Observation over Guangzhou. *Journal of Tropical Meteorology*, 27(3), 303-318. doi: https://doi.org/10.46267/j.1006-8775.2021.027

Vilà-Guerau de Arellano, J., Van Heerwaarden, C. C., Van Stratum, B. J., & Van den Dries, K. (2015). Atmospheric boundary layer: Integrating air chemistry and land interactions. Cambridge University Press.

You, C., & Chi-Hung Fung, J. (2019). Characteristics of the sea-breeze circulation in the Pearl River Delta region and its dynamical diagnosis. *Journal of Applied Meteorology and Climatology*, 58(4), 741-755. doi: https://doi.org/10.1175/JAMC-D-18-0153.1

Geophysical Research Letters

Supporting Information for

Rethinking the role of transport and photochemistry in regional ozone pollution: Insights from ozone mass and concentration budgets

K. Qu[1,2,3], X. Wang[1,2,*], X. Cai[1,2], Y. Yan[1,2], X. Jin[1,2], M. Vrekoussis[3,4,5], J. Shen[6], T. Xiao[1,2], L. Zeng[1,2] and Y. Zhang[1,2,7,8,*]

[1] State Key Joint Laboratory of Environmental Simulation and Pollution Control, College of Environmental Sciences and Engineering, Peking University, Beijing 100871, China.

[2] International Joint Laboratory for Regional Pollution Control, Ministry of Education, Beijing, 100816, China.

[3] Laboratory for Modeling and Observation of the Earth System (LAMOS), Institute of Environmental Physics (IUP), University of Bremen, Bremen, Germany.

[4] Center of Marine Environmental Sciences (MARUM), University of Bremen, Germany.

[5] Climate and Atmosphere Research Center (CARE-C), The Cyprus Institute, Cyprus.

[6] State Key Laboratory of Regional Air Quality Monitoring, Guangdong Key Laboratory of Secondary Air Pollution Research, Guangdong Environmental Monitoring Center, Guangzhou 510308, China.

[7] Beijing Innovation Center for Engineering Science and Advanced Technology, Peking University, Beijing 100871, China.

[8] CAS Center for Excellence in Regional Atmospheric Environment, Chinese Academy of Sciences, Xiamen 361021, China.

Corresponding author: X. Wang (xswang@pku.edu.cn) and Y. Zhang (yhzhang@pku.edu.cn)

Contents of this file

Introductions

Four texts, 12 figures and two tables are included in this Supporting Information for the paper entitled “Rethinking the role of transport and photochemistry in regional ozone pollution: Insights from ozone mass and concentration budgets”.

For text:

- Text S1 describes the detailed process of O_3 budget calculations in this study.
- Text S2 is the comparison between the equations of O_3 budget calculations used in this study with these in 1-D models.
- Text S3 presents the results of model validation of atmospheric boundary layer (ABL) height, wind and O_3 mixing profiles based on the IAGOS dataset.
- Text S4 gives further analyses on the contributions of horizontal transport and ABL-free troposphere (FT) exchange due to the large-scale air motions (ABL-FT-M; advection through the ABL top) in O_3 mass and concentration budgets.

For figures:

- Figure S1 indicates two calculation paths in the calculation of regional O_3 concentration budget within an hour.
- Figure S2 shows the results of O_3 budget closure examinations for O_3 mass and concentration budgets in the two representative months.
- Figure S3 displays the spatial distributions of the second modeling domain (d02) and source regions.
- Figure S4 presents the spatial distributions of 18 sites of the Guangdong-Hong Kong-Macao Pearl River Delta Regional Air Quality Monitoring Network.
- Figure S5 compared the mean diurnal changes of O_3 concentrations in the Pearl River Delta from three sources: observational near-ground O_3 concentrations, modeling near-ground O_3 concentrations and modeling ABL-mean O_3 concentrations.
- Figure S6 is the flow diagram of the O_3 budget calculation processes.
- Figure S7 is the flow diagram of the O_3 budget calculation in the Step I (or the tool *flux_4d_cal*).
- Figure S8 shows the comparison results between IAGOS and modeling atmospheric boundary layer height in Hong Kong in Oct. 2015.
- Figure S9 shows the comparisons between IAGOS and modeling wind roses in Hong Kong in the two representative months.
- Figure S10 shows the comparisons between IAGOS and CMAQ modeling vertical profiles of O_3 mixing ratios in Hong Kong in the two representative months.
- Figure S11 displays the wind roses at 14:00, 16:00, and 18:00 local time of O_3 polluted days in July 2016 in the Pearl River Delta.
- Figure S12 displays the cross-section of O_3 concentrations and wind fields at 16:00 local time on a representative polluted day of July 2016.

For tables:

- Table 1 gives more detailed information on the O_3 polluted days of the Pearl River Delta in the two representative months.
- Table 2 lists the formulas in the O_3 flux calculations, parameters used and their source files in the *flux_4d_cal* tool.

Text S1. Detailed process of O_3 budget calculations

As the flow diagram shown in Fig. S6, there are two steps in the calculations of O_3 budget based on the WRF-CMAQ modeling results:

1) Step I: Quantifications of transport fluxes and volume

The post-processing tool *flux_4d_cal* was developed using FORTRAN90 for this step. For all grids except for those next to the boundaries of the modeling domain, the calculation contents in the tool include:

- Hourly horizontal transport fluxes of O_3 within the ABL, including these in the x- and y-directions;
- Hourly fluxes of O_3 attributed to ABL-FT exchange due to the changes of ABL heights (ABL-FT-H);
- Hourly fluxes of O_3 attributed to ABL-FT exchange due to the large-scale air motion (advection through the ABL top; ABL-FT-M), including these in the x-, y- and z-directions;
- Hourly contributions of other processes (gas-phase chemistry, cloud process and dry deposition) to O_3 mass variations within the ABL;
- Hourly transported air volumes by each transport process;
- Total O_3 masses within the ABL at both the start and end of each hour;
- ABL heights at the starting and end hours.

(Note: ABL, atmospheric boundary layer; FT, free troposphere.)

All of the above values can be found in the netcdf (nc) output files, and they are used in the Step II calculations.

To finish the calculations of Step I, several input files are needed:

- Meteorological files processed by the MCIP module in CMAQ from the WRF outputs, which include the METCRO2D (meteorological parameters in the 2-D space), METCRO3D (meteorological parameters in the 3-D space) and MERDOT3D (wind speeds in the 3-D space) files;
- Pollutant concentration output files (CONC files) modeled by CMAQ, where hourly O_3 concentrations are stored;
- Process Analysis (PA) output files modeled by CMAQ, where the hourly, nested contributions of gas-phase chemistry, cloud process and dry deposition to O_3 concentration are stored.

For most of the files used here, the setting of spatial domains and times should be consistent; otherwise, the calculations would not be performed or generate wrong results. Additionally, users should provide the resolution of the modeling domain and the orders of contributions by three non-transport O_3 processes in the PA files for further calculations.

The flow chart of the calculation in *flux_4d_cal* is shown in Fig. S7. The calculation formulas for the grid cell (i, j), parameters used and their source files are summarized in Table S2. There are four loops in the calculations, which are the loops of x-, y-grids, time steps and vertical layers. We assume that there are 60 time-steps within an hour, and parameters at each time step can be

interpolated linearly by their values at the starting and end hours. The hourly contribution of non-transport processes to O_3 in a grid cell is divided equally to these within each time step. For every layer within the ABL, fluxes and volumes related to horizontal transport and non-transport processes are calculated and summed up. For layers where the ABL top is located, besides these aforementioned parameters, fluxes and volumes related to ABL-FT exchange (ABL-FT-H and ABL-FT-M) are also calculated. Total O_3 masses within the ABL at the start and end of each hour are directly calculated, and ABL heights at the starting and end hours can be read from the METCRO2D files.

The height of night-time stable ABL can be severely underestimated by normally used ABL parameterization, especially when the Richardson number is used (Dai et al., 2014). To reduce the influence of imprecise ABL heights in the O_3 budget calculations, here, we set the lowest ABL height limit as 350 m for all hours, which is an approximate value close to the values reported by night-time observations in summer or autumn in the Pearl River Delta (Chan et al., 2006; Fan et al., 2011; He et al., 2021; Song et al., 2021). The results of budget closure examination (Fig. S2) also suggest that the choice of this value is acceptable. Further studies are surely needed to better determine this value. However, we focus on the causes of daytime ozone pollution; thus, night-time budgets do not notably influence the conclusions of this study.

2) <u>Step II: Regional O_3 budget calculations and closure examinations</u>

This step aims to: 1) calculate the hourly O_3 mass and concentration budgets within the ABL of the user-defined regions, and 2) check whether the closure between the changes of O_3 masses/concentrations modelled by CMAQ and the net contributions of processes calculated above can be achieved. Besides the nc file generated in Step I, the definition of targeted region grids and borders (the grids within the targeted region and adjacent to the outside regions) should also be provided by users. Any software with basic data analysis and nc-file processing (Python, MATLAB, R, etc.) can be applied for this step.

The calculation processes in this step include:

- Calculation of the hourly horizontal transport fluxes of O_3 through each user-defined border (O_3 fluxes in every interface between the border grids and the outside regions, in both x- and y-directions, are taken into the calculations).
- Calculation of the hourly ABL-FT exchange fluxes of O_3 and the contributions of other processes to O_3 mass within user-defined targeted region grids.
- Calculation of the hourly O_3 concentration budget (the contributions of processes to the hourly variations of O_3 concentrations) based on O_3 transport fluxes and the corresponding volumes of transported air parcels.

More details on the calculation of the O_3 concentration budget are introduced as follows. As displayed in Fig. S1, within an hour, the mean O_3 concentration within the ABL of the targeted region changes from c_0 to c_1. Normally, O_3 mass and ABL volume both change notably, making it difficult to quantify the contributions to O_3 concentration variations by various processes. It should be noted that this is one of the main reasons why regional O_3 mass and concentration budgets are different. To simplify the calculation, two calculation paths (shown as the red arrowlines in Fig. S1; c_{r1} and c_{r2} are the reference O_3 concentrations separately for two calculation paths) are used in the calculations, assuming that only O_3 mass or ABL volume change in each step of two paths. For the path "$c_0 \Rightarrow c_{r1} \Rightarrow c_1$", the first step is the ABL volume change step, with O_3 concentration change described as:

$$c_{r1} - c_0 = c_0 \times \left(\frac{\sum H_0}{\sum H_1} - 1\right) \tag{S1}$$

where H_0 and H_1 are the ABL heights at the starting and end hours. It is counted as part of the contributions by ABL-FT-H. The second step is the O_3 mass change step, with O_3 concentration change described as:

$$\begin{aligned} c_1 - c_{r1} = & \frac{\sum(F_{htrans} - c_{r1} \times \Delta V_{htrans})}{L^2 \times \sum H_1} \\ & + \frac{\sum(F_{ABL-FT-M} - c_{r1} \times \Delta V_{ABL-FT-M})}{L^2 \times \sum H_1} + \frac{F_{ABL-FT-H}}{L^2 \times \sum H_1} \\ & + \frac{F_{chem}}{L^2 \times \sum H_1} + \frac{F_{cloud}}{L^2 \times \sum H_1} + \frac{F_{ddep}}{L^2 \times \sum H_1} \end{aligned} \tag{S2}$$

where F_{htrans}, $F_{ABL-FT-M}$, $F_{ABL-FT-H}$, F_{chem}, F_{cloud} and F_{ddep} indicate the contributions of horizontal transport, ABL-FT-M, ABL-FT-H, gas-phase chemistry, cloud process and dry deposition, respectively, to O_3 mass change. ΔV_{htrans} and $\Delta V_{ABL-FT-M}$ are the volumes of transported air parcel attributed to horizontal transport and ABL-FT-M, respectively, within an hour. L denotes the length of the grid cell, or the horizontal resolution of the model. The six terms on the right-hand sides of the above formula are separately classified as the individual contribution of horizontal transport, ABL-FT-M, ABL-FT-H, gas-phase chemistry, cloud process and dry deposition in the O_3 concentration budgets. Note that the contributions of ABL-FT-H are separately calculated in two steps. Similarly, for the path "c_0 => c_{r2} => c_1", the changes of O_3 concentration in two steps can be described as:

$$\begin{aligned} c_{r2} - c_0 = & \frac{\sum(F_{htrans} - c_0 \times \Delta V_{htrans})}{L^2 \times \sum H_0} \\ & + \frac{\sum(F_{ABL-FT-M} - c_0 \times \Delta V_{ABL-FT-M})}{L^2 \times \sum H_0} + \frac{F_{ABL-FT-H}}{L^2 \times \sum H_0} \\ & + \frac{F_{chem}}{L^2 \times \sum H_0} + \frac{F_{cloud}}{L^2 \times \sum H_0} + \frac{F_{ddep}}{L^2 \times \sum H_0} \end{aligned} \tag{S3}$$

$$c_1 - c_{r2} = c_{r2} \times \left(\frac{\sum H_0}{\sum H_1} - 1\right) \tag{S4}$$

The contributions of various processes can be classified correspondingly. The final results of contributions by processes are the average values of these calculated based on two calculation paths.

Text S2. Comparisons of O_3 concentration budget calculations between this study and 1-D models

When the region column in the Chemical Transport Models (CTMs) is thin enough to resemble a line, the O_3 concentration budget calculations using the CTMs results are expected to be the same as those in 1-D models. Thus, we can use it to check the validity of O_3 concentration budget calculations in this study.

Here the contributions of horizontal transport to the variations of O_3 concentration over the studied space ($\langle c \rangle$) can be described as (Eq. (3) in the manuscript):

$$\left[\frac{\partial \langle c \rangle}{\partial t}\right]_{htrans} = \frac{F_{htrans} + \langle c \rangle (V - dV)}{V} - \langle c \rangle = \frac{F_{htrans} - \langle c \rangle dV}{V} \tag{S5}$$

where F_{htrans} is the O_3 flux of horizontal transport; V is the original volume of the PRD grids below the ABL; dV is the volume of transported parcels. Assume that the length of the region in the x-directions is dx, thus,

$$V = S\,dx \tag{S6}$$

where S is the area of the interface. As calculated in the O_3 mass budget, in the unit time,

$$F_{htrans} = cuS \tag{S7}$$

$$dV = uS \tag{S8}$$

where c is O_3 concentration in the transported air parcels, and u is the mean horizontal wind speed in the interface. Therefore, from Eqs. (S5)-(S8), we can get:

$$\left[\frac{\partial\langle c\rangle}{\partial t}\right]_{htrans} = u\frac{\mathrm{c}-\langle c\rangle}{dx} = u\frac{dc}{dx} \tag{S9}$$

For ABL-FT-H, its contributions when V is much higher than dV (this assumption can be normally met when the period is short) are:

$$\left[\frac{\partial\langle c\rangle}{\partial t}\right]_{ABL-FT-H} = \frac{F_{ABL-FT-H}+\langle c\rangle V}{V+dV} - \langle c\rangle \approx \frac{F_{ABL-FT-H}-\langle c\rangle dV}{V} \tag{S10}$$

where $F_{ABL-FT-H}$ is the O_3 flux contributed by ABL-FT-H. In the unit time,

$$F_{ABL-FT-H} = c_h\frac{\partial H}{\partial t}L^2 \tag{S11}$$

$$dV = \frac{\partial H}{\partial t}L^2 \tag{S12}$$

$$V = HL^2 \tag{S13}$$

where c_h is the O_3 concentration in the ABL top; L is the width of the grid cell (equal to the horizontal resolution of the model); H is the ABL height. Therefore, from Eqs. (S10)-(S13),

$$\left[\frac{\partial\langle c\rangle}{\partial t}\right]_{ABL-FT-H} = \frac{c_h-\langle c\rangle}{H}\frac{\partial H}{\partial t} \tag{S14}$$

For ABL-FT-M,

$$\begin{aligned}\left[\frac{\partial\langle c\rangle}{\partial t}\right]_{ABL-FT-M} &= \frac{F_{ABL-FT-M}+\langle c\rangle(V-dV)}{V} - \langle c\rangle \\ &= \frac{F_{ABL-FT-M}-\langle c\rangle dV}{V}\end{aligned} \tag{S15}$$

$F_{ABL-FT-M}$ is the O_3 flux attributed to ABL-FT-M. In the unit time,

$$F_{ABL-FT-M} = c_h\left(u_h\frac{\partial H}{\partial x} + v_h\frac{\partial H}{\partial y} - w_h\right)L^2 \tag{S16}$$

$$dV = \left(u_h\frac{\partial H}{\partial x} + v_h\frac{\partial H}{\partial y} - w_h\right)L^2 \tag{S17}$$

$$V = HL^2 \tag{S18}$$

where u_h, v_h and w_h are the ABL-top wind speeds in the x, y and z-direction, respectively. Therefore, from Eq. (S15-18),

$$\left[\frac{\partial\langle c\rangle}{\partial t}\right]_{ABL-FT-M} = \frac{c_h - \langle c\rangle}{H}\left(u_h\frac{\partial H}{\partial x} + v_h\frac{\partial H}{\partial y} - w_h\right) \tag{S19}$$

$$\begin{aligned}\left[\frac{\partial\langle c\rangle}{\partial t}\right]_{ABL-FT} &= \left[\frac{\partial\langle c\rangle}{\partial t}\right]_{ABL-FT-H} + \left[\frac{\partial\langle c\rangle}{\partial t}\right]_{ABL-FT-M} \\ &= \frac{c_h - \langle c\rangle}{H}\left(\frac{\partial H}{\partial t} + u_h\frac{\partial H}{\partial x} + v_h\frac{\partial H}{\partial y} - w_h\right) = \frac{w_e\Delta c}{H}\end{aligned} \tag{S20}$$

where w_e is the entrainment rate of the ABL; Δc is equal to the difference between O_3 concentrations in the FT and ABL. Therefore, for these transport processes, the above formulas (Eqs. (S9), (S14), (S19), and (S20)) are the same as those used in 1-D models (Janssen and Pozzer, 2015; Vilà-Guerau de Arellano et al., 2015), suggesting their applicability in the quantification of the O_3 concentration budget using CTMs modeling results.

Text S3. Model validation of ABL height, wind and O_3 mixing ratio profiles based on the IAGOS dataset

IAGOS (In-service Aircraft of a Global Observing System; https://www.iagos.org) is a global aircraft-based observing system, where state-of-the-art instruments deployed in aircrafts are used to measure reactive gases, greenhouse gases, aerosol and clouds in the troposphere and lower stratosphere (Petzold et al., 2016). Meteorological parameters, including air temperature, wind speed and direction, are also provided by IAGOS. When the aircrafts climb up or descent, these measurements are suitable for obtaining the vertical profiles of parameters with high resolutions, which provides valuable observational datasets for the model validation in the vertical direction.

To ensure reasonable quantifications of the O_3 budgets, the IAGOS dataset in two representative months in Hong Kong (located in the south PRD) was used to evaluate the modeling performance of WRF-CMAQ in this study. We focused on comparing parameters within the height range of 0-5 km. Since observational data is often missing in some height ranges and the vertical resolution of modeling results is relatively low, we calculated the mean observational and modeling values within every 500 m height range (i.e., 0-500 m, 500-1000 m, etc.) for the comparisons. The detailed evaluations are introduced as follows:

(1) Atmospheric boundary layer (ABL) heights:

ABL heights are used to quantify the contribution of ABL-FT exchange in the O_3 budgets. Therefore, the evaluation of modeled ABL heights is important. In this study, the observational ABL heights were determined using the profiles of potential temperature (θ) in IAGOS, defined as the heights where the lapse rate of θ ($\partial\theta/\partial z$, the rate of θ changing over height change) reaches its maximum values (Dai et al., 2014). Since there are limited profiles available in July 2016 and night-time ABL heights are hard to be accurately determined, we only evaluated the modeling performance of ABL heights during the daytime (6:00-18:00 Local Time (LT)) of Oct. 2015. As shown in Fig. S8, the mean bias (MB) between modeling and observational ABL heights in Hong Kong is only -1.1 m, and a good correlation between ABL heights from two datasets (R = 0.76) suggests that the mean diurnal cycles of ABL can be modeled well. Though the modeling performance of ABL heights is satisfying based on the IAGOS dataset in Hong Kong, more comprehensive comparisons based on three-dimensional observations with higher spatiotemporal resolutions and coverages are required for more accurate O_3 budget estimates in future studies.

(2) Wind profiles:

Figure S9 shows the IAGOS and modeling wind roses within the height ranges of 0-1000 m, 1000-2000 m and 2000-5000 m. Both datasets indicate that higher wind speed can be generally found at higher altitudes. In autumn, WRF overestimates wind speed below 1000 m by 0.6 m/s (16%), but underestimates it above 1000 m. In summer, the biases between wind speeds in the two datasets are relatively smaller, especially at lower heights (< 2000 m). Both datasets show similar prevailing wind directions at different height ranges and in different seasons. Thus, the modeling performance of wind speeds and directions in the vertical direction is acceptable.

(3) O_3 mixing ratio profiles:

The comparisons between observational and modeling profiles of O_3 mixing ratio are displayed in Fig. S10. Not many O_3 profiles were available in July 2016, and the useable ones were mostly measured during clean periods. Thus, the comparison was mainly based on the results in Oct. 2015 (the number of IAGOS O_3 profiles available for the comparisons is 41). Both datasets show that O_3 mixing ratio decreases with height in Hong Kong. Below the height of 1000 m, the observational and modeling O_3 mixing ratios are 71.4 ppbv and 75.8 ppbv, respectively. Within the height range of 1000-2000 m, the O_3 mixing ratio is overestimated by 26%. High O_3 levels during Oct. 13-24 and relatively low O_3 levels in other periods can be found in both datasets, suggesting that the developments of O_3 pollution in the month were modeled well. Therefore, the performance of O_3 profiles modeling can also meet the requirement of O_3 budget calculations.

Text S4. Further analyses on the contributions of horizontal transport and ABL-FT-M in O_3 mass and concentration budgets

(Note: ABL-FT-M, the exchange between ABL and FT due to large-scale air motions (advection through the ABL top).)

As shown in Fig. 3 in the manuscript of this paper, the contributions of both horizontal transport and ABL-FT-M in both O_3 budgets were less notable than those of ABL-FT-H and gas-phase chemistry. However, they reflect the characteristics of regional wind fields, thus are still worthy of further analyses. Two main findings are described as follows:

(1) <u>The contribution of horizontal transport and ABL-FT-M in autumn is connected to the characteristics of horizontal wind fields in the PRD.</u>

Northerly and easterly winds prevail in autumn (Fig. S9), thus O_3 is transported into the PRD through its north and east borders, out of the PRD through the south and west borders, which has been shown in the results of the O_3 mass budget. O_3 outfluxes were generally higher than influxes in the daytime, which is attributed to higher O_3 levels in the air parcels transported out of the PRD than these in parcels into the region. This is also why horizontal transport leads to the decrease of O_3 concentration in the daytime. Though horizontal transport contributed to lower O_3 fluxes at night, it became the main nighttime source for O_3. This is to say, the transport of air parcels with high O_3 levels from the outskirts helped maintain O_3 pollution in the PRD to some extent at night.

The contributions of ABL-FT-M are related to the prevailing of northerly winds in the PRD. The PRD has mountainous regions in the northern, western and eastern outskirts, as well as urban regions with lower altitudes in the central plain. Thus, north winds resulted in the downward transport of O_3 along the terrain. Daytime ABL heights in urban regions were, in general, higher than those in mountainous regions, which is the other reason why O_3 can be easily transported

through the ABL top in the urban-rural interfaces when north wind prevailed. ABL-FT-M contributed to the increase of O_3 concentration during several hours after sunrise and the decrease of O_3 concentration in the afternoon, which is attributed to different comparison results between ABL and FT O_3 levels in two periods (ABL < FT in the morning; ABL > FT in the afternoon).

(2) <u>The contribution of horizontal transport and ABL-FT-M in summer indicates the influence of sea breezes in the PRD.</u>

Although southerly winds normally prevail in summer in the PRD (Fig. S9), on O_3 polluted days, air parcels from other directions could potentially influence the region as well (Qu et al., 2021), resulting in relatively lower horizontal transport fluxes of O_3 in comparison to these in autumn. What interests us is the different contributions of horizontal transport through the southern border of the PRD before and after ~14:00 LT. Besides, we also found high O_3 fluxes contributed by ABL-FT-M in the afternoon. These phenomena are both related to the influence of sea breezes in the PRD.

Figure S11 shows the near-ground wind roses at 14:00, 16:00 and 18:00 LT of O_3 polluted days in July 2016 based on the observational and modeling results in national meteorological sites within the PRD. At 14:00 LT, the main wind directions were W, SW and NW in both datasets. More S and SE winds occurred in later hours, and they became the prevailing winds at 18:00 LT — it suggests the gradual development of sea breezes in the PRD. Thus, O_3 was originally transported out of the PRD through its south border (O_3 fluxes < 0), but sea breezes gradually reversed the directions of O_3 transport, finally resulting in positive O_3 fluxes through the south border in the late afternoon. Sea breezes resulted in the changes of not only horizontal wind fields, but also vertical wind fields. Take the O_3 polluted day July 24th for example, and the cross-section of O_3 concentrations and wind fields in the PRD at 16:00 LT is shown in Fig. S12 (cross-sections were made along the 113.2° E latitude line, from 26.0 to 20.0° N). Sea breezes can be found in this plot, characterized by strong southerly wind and lower O_3 concentrations in the south part of the PRD. In regions where sea breezes and local air parcels encountered (characterized by the interface between low and high O_3 levels), updrafts occurred, suggesting the formation of sea breeze front (Ding et al., 2004; You and Fung, 2019). It promoted the upward transport of O_3 from the ABL to the FT, or considerable O_3 outfluxes attributed to ABL-FT-M.

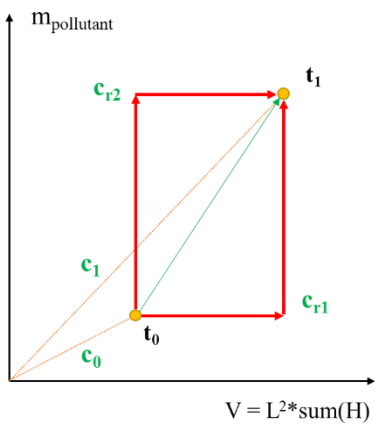

Figure S1. Two calculation paths in the calculation of regional O_3 concentration budget within an hour. $m_{pollutant}$ indicates the total mass of pollutants in the atmospheric boundary layer (ABL) of the studied region; V is the volume of the ABL of the region; L is the length of the grids (equal to the horizontal resolution of the model); H is the ABL heights; t_0 and t_1 are the starting and end hours; c_0 and c_1 are the concentrations of pollutants in t_0 and t_1, respectively; c_{r1} and c_{r2} are the reference concentrations of pollutants for two calculation paths.

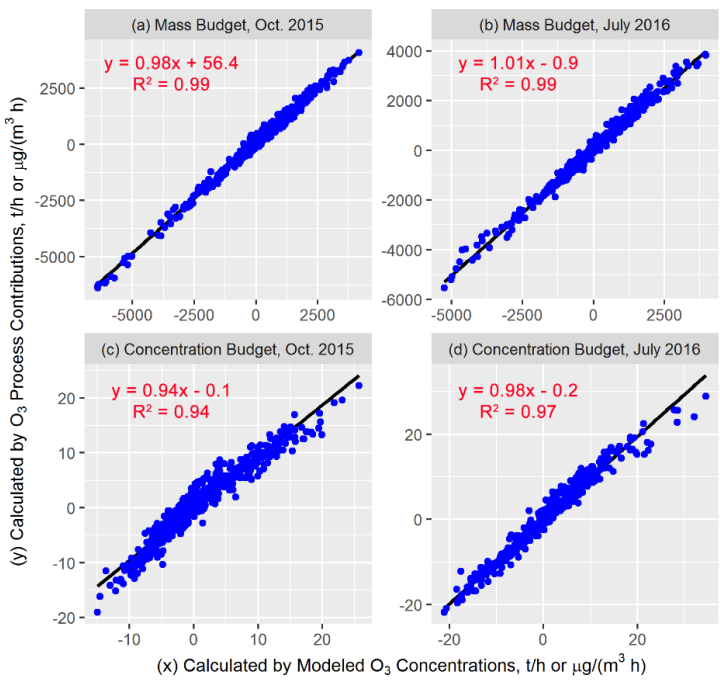

Figure S2. O_3 budget closure examinations in Oct. 2015 (a,c) and July 2016 (b,d), for the O_3 mass budget (a-b) and concentration budget (c-d). The units for the O_3 mass and concentration budgets are t/h and μg/(m^3 h), respectively.

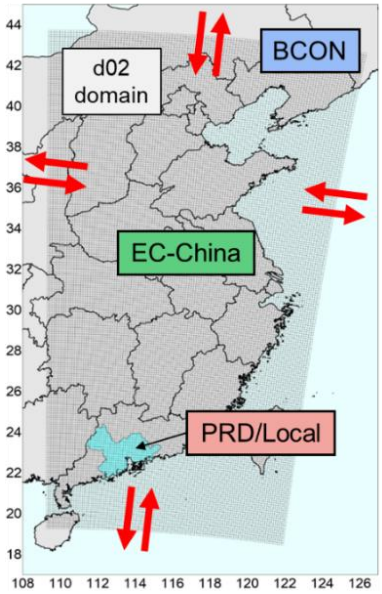

Figure S3. The spatial distributions of the d02 modeling domain and source regions. PRD, Pearl River Delta; EC-China, East and Central China; BCON, the boundary conditions of d02 modeling, or the contributions of sources outside d02.

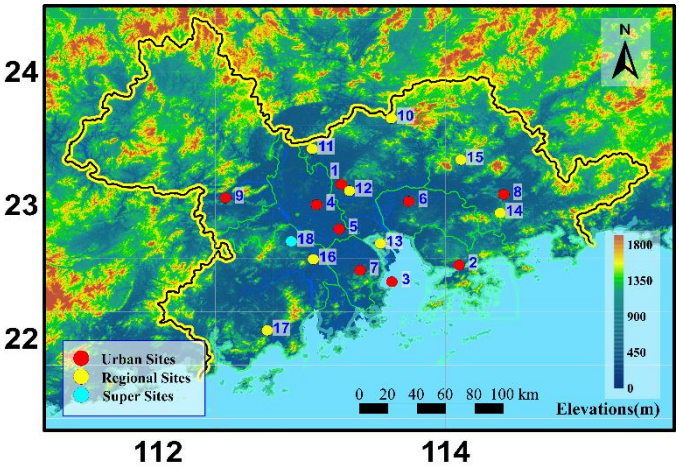

Figure S4. Spatial distributions of 18 sites of the Guangdong-Hong Kong-Macao Pearl River Delta Regional Air Quality Monitoring Network. The names of all sites and their located municipalities are: 1. Luhu, Guangzhou; 2. Liyuan, Shenzhen; 3. Tangjia, Zhuhai; 4. Huijingcheng, Foshan; 5. Jinjuju, Foshan; 6. Nanchengyuanling, Dongguan; 7. Zimaling, Zhongshan; 8. Xiapu, Huizhou; 9. Chengzhongzizhan, Zhaoqing; 10. Tianhu, Guangzhou; 11. Zhudong, Guangzhou; 12. Modiesha, Guangzhou; 13. Wanqingsha, Guangzhou; 14. Jinguowan, Huizhou; 15. Xijiao, Huizhou; 16. Donghu, Jiangmen; 17. Duanfen, Jiangmen; 18. Heshan Supersite, Jiangmen.

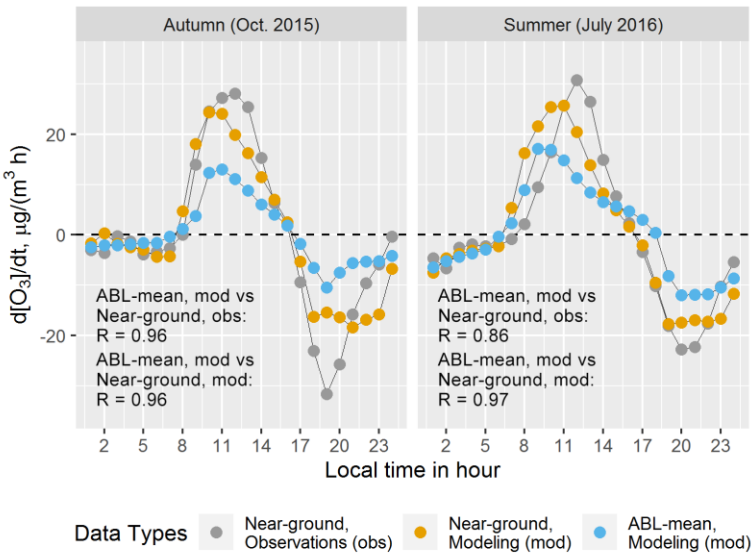

Figure S5. Mean diurnal change of the hourly variations of observational, modeling mean near-ground O_3 concentrations in 18 sites of the Guangdong-Hong Kong-Macao regional monitoring network and modeling mean O_3 concentration over the atmospheric boundary layer (ABL) of the Pearl River Delta on the polluted days of autumn (Oct. 2015) and summer (July 2016).

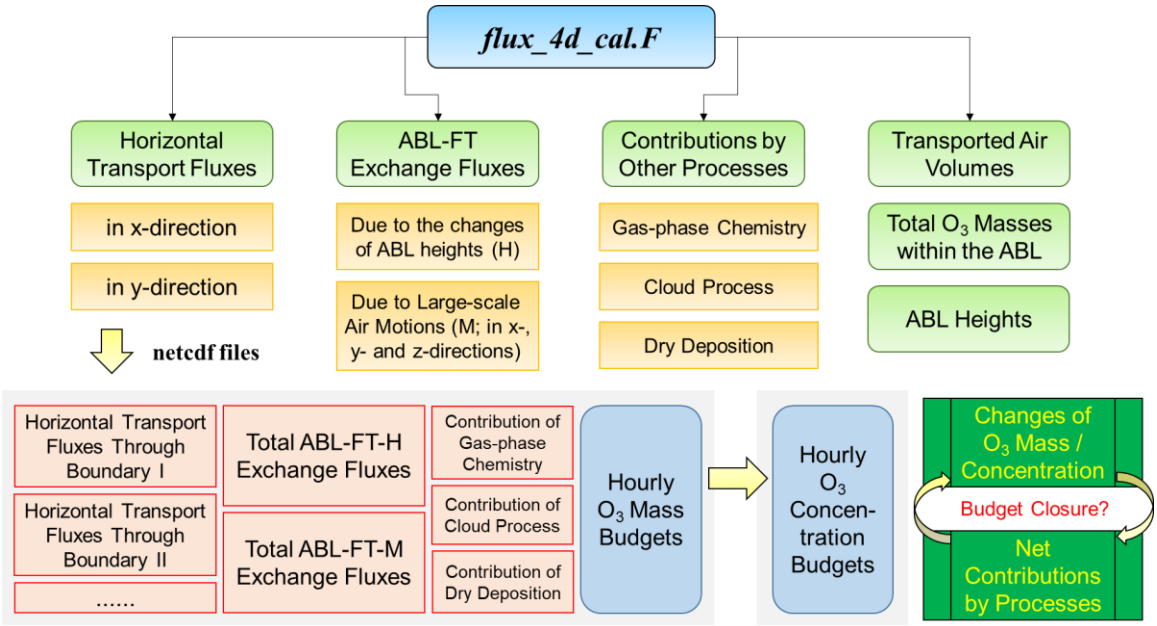

Figure S6. Flow diagram of the O_3 budget calculation processes. ABL, atmospheric boundary layer; FT, free troposphere; ABL-FT-H, ABL-FT exchange due to the changes of ABL height; ABL-FT-M, ABL-FT exchange due to the large-scale air motions (advection through the ABL top).

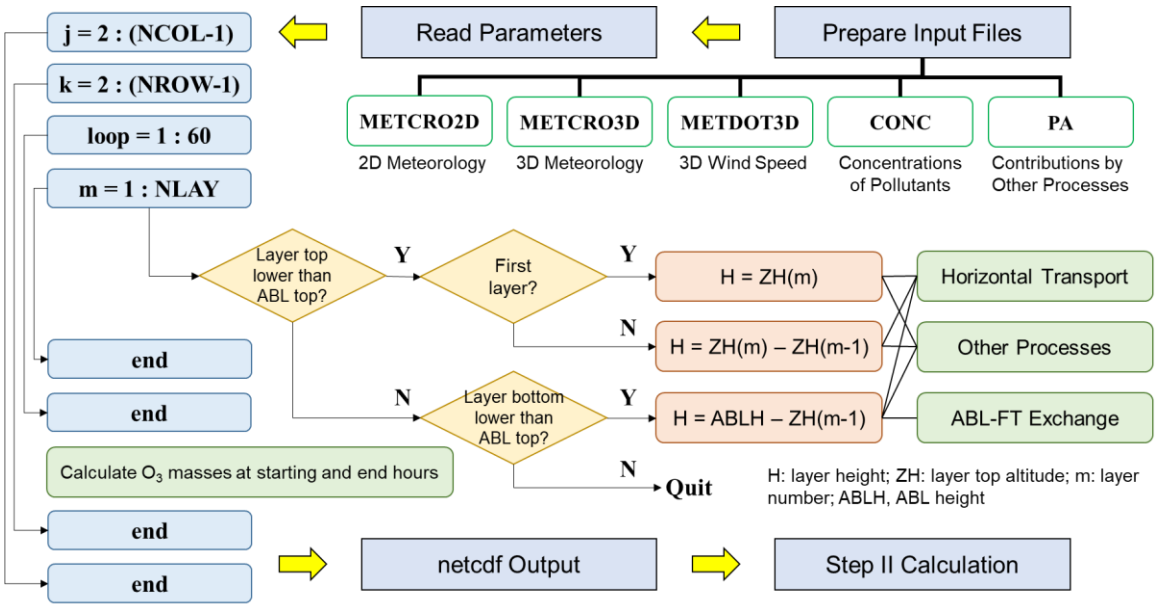

Figure S7. Flow diagram of the O_3 budget calculation in the Step I (or the tool *flux_4d_cal*). NCOL, NROW and NLAY indicate the number of columns, rows and vertical layers in the modeling domain. ABL, atmospheric boundary layer; FT, free troposphere. METCRO2D, 2-dimensional meteorological outputs from the MCIP module in CMAQ; METCRO3D, 3-dimensional meteorological outputs from the MCIP module in CMAQ; METDOT3D, 3-dimensional wind fields outputs from the MCIP module in CMAQ; CONC, 3-dimensional outputs of pollutant concentrations from CMAQ; PA, 3-dimensional outputs of hourly contributions by three non-transport processes to O_3 from CMAQ.

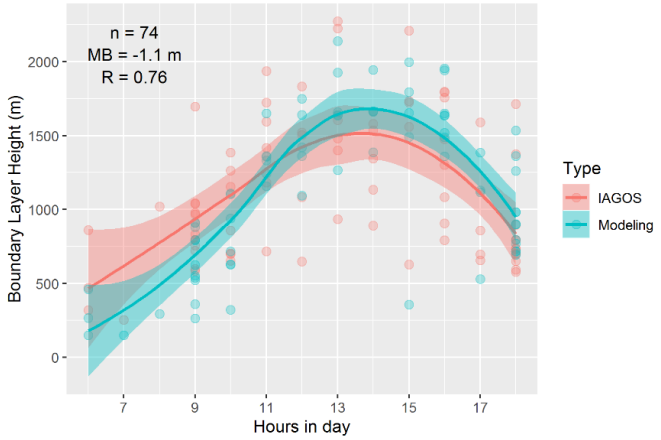

Figure S8. Comparisons between IAGOS and modeling atmospheric boundary layer height in Hong Kong in Oct. 2015. n, the number of available dataset for the comparison; MB, mean bias; R, correlation factor.

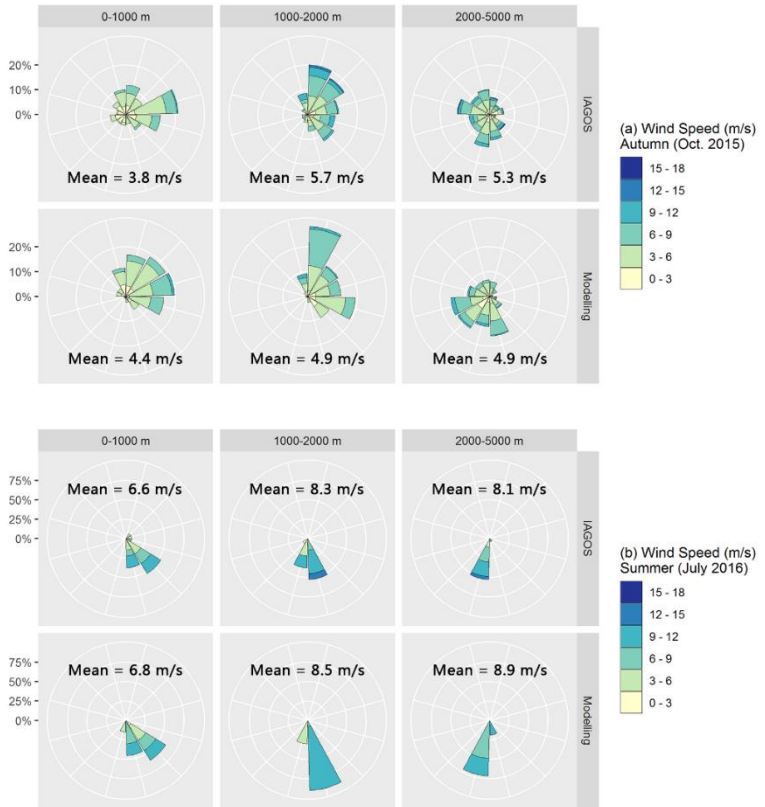

Figure S9. Comparisons between IAGOS and modeling wind roses in Hong Kong in (a) Oct. 2015 and (b) July 2016. Results within the height range of 0-1000 m, 1000-2000 m, and 2000-5000 m were separately displayed.

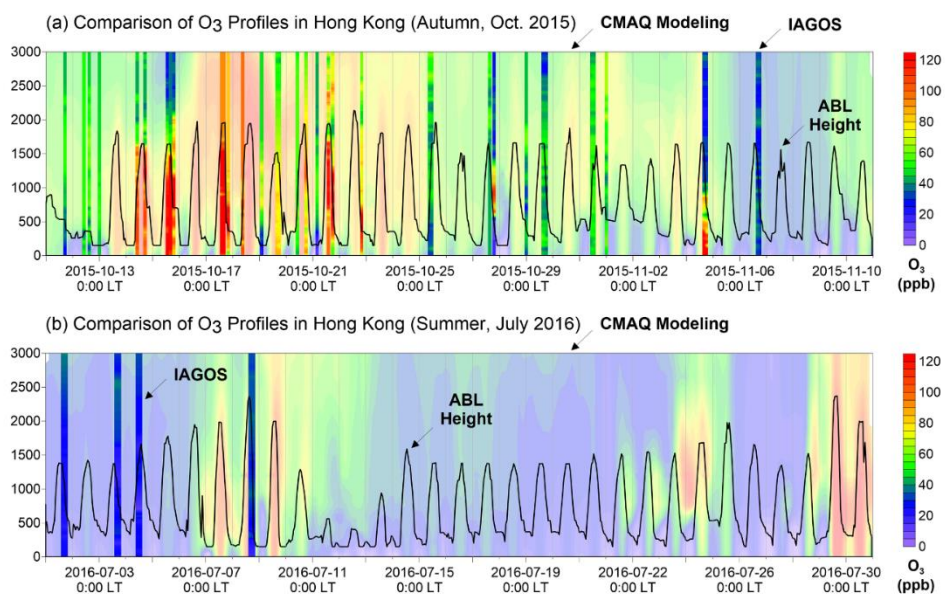

Figure S10. Comparisons between IAGOS and CMAQ modeling vertical profiles of O_3 mixing ratios (ppb) in Hong Kong in (a) Oct. 2015 and (b) July 2016. The heights of atmospheric boundary layer (ABL) modeled by WRF in two months are also shown as solid black lines.

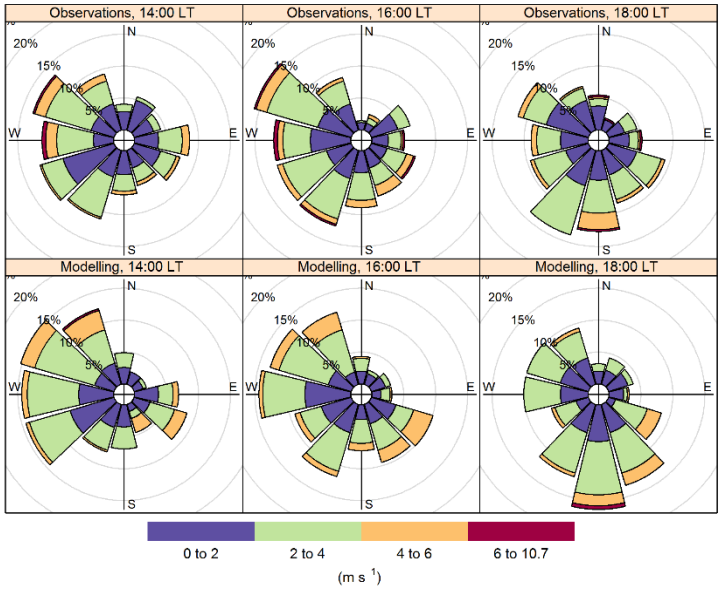

Figure S11. Wind roses at 14:00, 16:00, and 18:00 local time (LT) of O_3 polluted days in July 2016 in the Pearl River Delta (PRD). Observational and modeling wind speeds and directions in 29 national meteorological sites within the PRD were used for this figure.

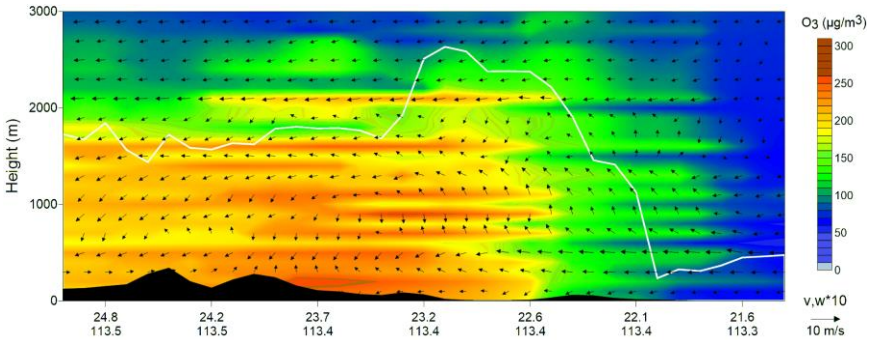

Figure S12. Cross-section of O_3 concentrations (μg/m^3) and wind fields at 16:00 local time on July 24th, 2016. The solid white line indicates the top of the atmospheric boundary layer.

Table S1. Information on the O_3 polluted days of the Pearl River Delta (PRD) in Oct. 2015 and July 2016. MDA1, the maximum 1-hr O_3 concentrations; MDA8, the maximum 8-hr average O_3 concentrations.

Dates	Influencing Weather Systems	O_3 concentrations in the PRD (the maximum values in nine municipals of the PRD, released by the China National Environmental Monitoring Centre; μg/m^3)	
		MDA1	MDA8
Oct.13, 2015	Typhoon Koppu and Champi	201	164
Oct.14, 2015		301	244
Oct.15, 2015		271	227
Oct.16, 2015		260	219
Oct.17, 2015		233	211
Oct.18, 2015		205	187
Oct.19, 2015		214	174
Oct.20, 2015		200	158
Oct.21, 2015		214	195
Oct.22, 2015		209	182
Oct.23, 2015		249	199
Oct.24, 2015		225	193
Oct.28, 2015	Subtropical High	238	186
Nov.3, 2015	Sea High	207	162
Nov.4, 2015		182	168
Nov.5, 2015		255	187
July 7, 2016	Typhoon Nepartak	297	256
July 8, 2016		260	198
July 9, 2016		263	231
July 10, 2016		211	150
July 22, 2016	Subtropical High	211	176
July 23, 2016		223	197
July 24, 2016		265	226
July 25, 2016		334	269
July 26, 2016		235	164
July 29, 2016		271	204
July 30, 2016	Typhoon Nida	268	187
July 31, 2016		385	344

Table S2. Formulas in the O_3 flux calculations for the grid cell (*i*, *j*) in the unit time *dt*, parameters used and their source files in the *flux_4d_cal* tool.

Processes	Formulas of O_3 fluxes	Parameters used	Sources of parameters
Horizontal transport (in the x-direction)	$F_{u-trans} = \sum_{k=1}^{h} c_{i-1,j} u_{i,j+\frac{1}{2}} L\Delta z dt$	$c_{i-1,j}$: O_3 concentrations in the grid cell (*i*-1, *j*)	CONC files
		$u_{i,j+\frac{1}{2}}$: wind speeds in the west interface	METDOT3D files
		L: the length of grid cells (= model resolution)	User defined
		Δz: layer heights ($H - z_{h-1}$ for the ABL top layer, $z_k - z_{k-1}$ for other layers within the ABL; H, ABL height)	METCRO3D files
		h: the layer of ABL top	Determined by ABL height
Horizontal transport (in the y-direction)	$F_{v-trans} = \sum_{k=1}^{h} c_{i,j-1} v_{i+\frac{1}{2},j} L\Delta z dt$	$c_{i,j-1}$: O_3 concentrations in the grid cell (*i*, *j*-1)	CONC files
		$v_{i+\frac{1}{2},j}$: wind speeds in the south interface	METDOT3D files
		L: the length of grid cells (= model resolution)	User defined
		Δz: layer heights ($H - z_{h-1}$ for the ABL top layer, $z_k - z_{k-1}$ for other layers within the ABL; H, ABL height)	METCRO3D files
		h: the layer of ABL top	Determined by ABL height
ABL-FT exchange due to the changes of ABL heights	$F_{ABL-FT-H} = c_h \frac{\partial H}{\partial t} L^2 dt$	c_h: O_3 concentrations in the ABL top layer	CONC files
		$\frac{\partial H}{\partial t}$: the change rates of ABL height	METCRO2D files
		L: the length of grid cells (= model resolution)	User defined
ABL-FT exchange due to large-scale air motions (in the x-direction)	$F_{ABL-FT-Cu} = c_{i-1,j(h)} u_{i,j+\frac{1}{2}(h)} \frac{\partial H}{\partial x} L^2 dt$	$c_{i-1,j(h)}$: O_3 concentrations in the ABL top layer of the grid cell (*i*-1, *j*)	CONC files
		$u_{i,j+\frac{1}{2}(h)}$: wind speeds in the ABL top layer of the west interface	METDOT3D files
		L: the length of grid cells (= model resolution)	User defined
		$\frac{\partial H}{\partial x}$: the difference of ABL heights in x-direction, or between the grid cells (*i*, *j*) and (*i*-1, *j*)	METCRO2D files
ABL-FT exchange due to large-scale air motions (in the y-direction)	$F_{ABL-FT-Cv} = c_{i,j-1(h)} v_{i+\frac{1}{2},j(h)} \frac{\partial H}{\partial y} L^2 dt$	$c_{i,j-1(h)}$: O_3 concentrations in the ABL top layer of the grid cell (*i*, *j*-1)	CONC files
		$v_{i+\frac{1}{2},j(h)}$: wind speeds in the ABL top layer of the south interface	METDOT3D files
		L: the length of grid cells (= model resolution)	User defined
		$\frac{\partial H}{\partial y}$: the difference of ABL heights in y-direction, or between the grid cells (*i*, *j*) and (*i*, *j*-1)	METCRO2D files
ABL-FT exchange due to large-scale air motions (in the z-direction)	$F_{ABL-FT-Cw} = -c_h w_h L^2 dt$	c_h: O_3 concentrations in the ABL top layer	CONC files
		w_h: vertical wind speeds in the ABL top layer	METCRO3D files
		L: the length of grid cells (= model resolution)	User defined
Other processes (gas-phase chemistry, cloud process, dry deposition)	$F_{others} = \sum_{k=1}^{h} IPR\Delta z dt$	IPR: integrated process rates of pre-set processes	PA files
		Δz: layer heights ($H - z_{h-1}$ for the ABL top layer, $z_k - z_{k-1}$ for other layers within the ABL; H, ABL height)	METCRO3D files
		h: the layer of ABL top	Determined by ABL height